



**HAL**  
open science

## Single-molecule imaging reveals distinct effects of ligands on CCR5 dynamics depending on its dimerization status

Fanny Momboisse, Giacomo Nardi, Philippe Colin, Melany Hery, Nelia Cordeiro, Olivier Schwartz, Nathalie Sauvonnet, Fernando Arenzana-Seisdedos, Thibault Lagache, Bernard Lagane, et al.

### ► To cite this version:

Fanny Momboisse, Giacomo Nardi, Philippe Colin, Melany Hery, Nelia Cordeiro, et al.. Single-molecule imaging reveals distinct effects of ligands on CCR5 dynamics depending on its dimerization status. 2022. pasteur-03821243v1

**HAL Id: pasteur-03821243**

**<https://pasteur.hal.science/pasteur-03821243v1>**

Preprint submitted on 27 Jun 2022 (v1), last revised 19 Oct 2022 (v2)

**HAL** is a multi-disciplinary open access archive for the deposit and dissemination of scientific research documents, whether they are published or not. The documents may come from teaching and research institutions in France or abroad, or from public or private research centers.

L'archive ouverte pluridisciplinaire **HAL**, est destinée au dépôt et à la diffusion de documents scientifiques de niveau recherche, publiés ou non, émanant des établissements d'enseignement et de recherche français ou étrangers, des laboratoires publics ou privés.



Distributed under a Creative Commons Attribution 4.0 International License

1

2

3 **Single-molecule imaging reveals distinct effects of ligands on**  
4 **CCR5 dynamics depending on its dimerization status**

5 Fanny Momboisse<sup>1</sup>, Giacomo Nardi<sup>2</sup>, Philippe Colin<sup>3</sup>, Melany Hery<sup>1</sup>, Nelia Cordeiro<sup>1</sup>,  
6 Olivier Schwartz<sup>1</sup>, Nathalie Sauvonnet<sup>5</sup>, Fernando Arenzana-Seisdedos<sup>4</sup>, Thibault  
7 Lagache<sup>2\*</sup>, Bernard Lagane<sup>3</sup>, Jean-Christophe Olivo-Marin<sup>2</sup>, Anne BreLOT<sup>1\*</sup>

8

9 <sup>1</sup> : Institut Pasteur, Université de Paris, CNRS UMR3569, Virus and Immunity Unit, F-  
10 75015 Paris, France.

11 <sup>2</sup> : Institut Pasteur, Université de Paris, CNRS UMR 3691, BioImage Analysis Unit, F-  
12 75015 Paris, France.

13 <sup>3</sup> : Infinity, Université de Toulouse, CNRS, INSERM, UPS, 31024 Toulouse Cedex 03,  
14 France.

15 <sup>4</sup> : Institut Pasteur, Université de Paris, INSERM U1108, Viral Pathogenesis Unit, F-  
16 75015 Paris, France.

17 <sup>5</sup> : Institut Pasteur, Université de Paris, Group Intracellular Trafficking and Tissue  
18 Homeostasis, F-75015 Paris, France.

19

20 \*To whom correspondence may be addressed:

21 **Email:** [anne.brelot@pasteur.fr](mailto:anne.brelot@pasteur.fr); [thibault.lagache@pasteur.fr](mailto:thibault.lagache@pasteur.fr)

22

23 **Competing Interests:** The authors declare that no competing interests exist.

24

25 **Abstract**

26 G protein-coupled receptors (GPCR) are present at the cell surface in different  
27 conformational and oligomeric states. However, how these states impact GPCRs  
28 biological function and therapeutic targeting remains incompletely known. Here, we  
29 investigated this issue in living cells for the CC chemokine receptor 5 (CCR5), a major  
30 receptor in inflammation and the principal entry co-receptor for Human  
31 Immunodeficiency Viruses (HIV-1). We used TIRF microscopy and an original statistical  
32 method to track and classify the motion of different receptors subpopulations. We  
33 showed a diversity of ligand-free forms of CCR5 at the cell surface constituted of various  
34 oligomeric states and exhibiting transient Brownian and restricted motions. These forms  
35 were stabilized differently by distinct ligands. In particular, agonist stimulation restricted  
36 the mobility of CCR5 and led to its clustering, a feature depending on  $\beta$ -arrestin, while  
37 inverse agonist stimulation exhibited the opposite effect. These results suggest a link  
38 between receptor activation and immobilization. Applied to HIV-1 envelope glycoproteins  
39 gp120, our quantitative analysis revealed agonist-like properties of gp120s. Distinct  
40 gp120s influenced CCR5 dynamics differently, suggesting that they stabilize different  
41 CCR5 conformations. Then, using a dimerization-compromized mutant, we showed that  
42 dimerization (i) impacts CCR5 precoupling to G proteins, (ii) is a pre-requisite for the  
43 immobilization and clustering of receptors upon activation, and (iii) regulates receptor  
44 endocytosis, thereby impacting the fate of activated receptors. This study demonstrates  
45 that tracking the dynamic behavior of a GPCR is an efficient way to link GPCR  
46 conformations to their functions, therefore improving the development of drugs targeting  
47 specific receptor conformations.

## 48 **Introduction**

49 G protein-coupled receptors (GPCRs), also known as 7TM (seven transmembrane  
50 helical) receptors, represent the largest group of cell surface receptors in humans that  
51 transduce chemical signals from the extracellular matrix into the cell. They constitute one  
52 of the primary drug target classes (Pierce et al., 2002).

53 GPCRs exist in different subpopulations at the cell surface, in part due to differential  
54 post-translational modifications (Patwardhan et al., 2021; Scurci et al., 2021) and  
55 arrangements of receptor loops and transmembrane domains (Deupi & Kobilka, 2010).  
56 Receptor activation and G protein coupling indeed involves a series of conformational  
57 changes from an inactive to an active state (Ahn et al., 2021). Coupling to different G  
58 proteins or to other protein transducers (e.g. arrestins), as well as receptor  
59 oligomerization expand the diversity of conformational states (Seyedabadi et al., 2019;  
60 Sleno & Hebert, 2018). Molecular dynamics along with biophysical and structural studies  
61 brought to light this variety of GPCR arrangements and showed how binding of different  
62 ligands can stabilize or select different receptor conformations, which can in turn activate  
63 different signaling pathways (Ahn et al., 2021). This concept of “functional selectivity” (or  
64 “biased agonism”) opens the possibility to develop therapies specifically targeting a  
65 selected receptor conformation, thereby increasing the effectiveness of drugs and  
66 reducing their adverse effects (Seyedabadi et al., 2019).

67 The nature and proportion of the different forms of GPCRs vary depending on their  
68 environment. This is likely to regulate the functional properties of the receptors (Colin et  
69 al., 2018; Patwardhan et al., 2021). Few studies, however, confirmed this diversity of  
70 receptors in living cells and investigated its regulation in time and space (Calebiro et al.,  
71 2013; Gormal et al., 2020; Kasai et al., 2018; Martinez-Munoz et al., 2018; Sungkaworn  
72 et al., 2017; Veya et al., 2015). In this study, we tracked the chemokine receptor CCR5

73 at the single molecule level to access its dynamic behavior at the plasma membrane and  
74 identify the stoichiometry and the functional properties of the various receptor forms.

75 CCR5 is a class A GPCR expressed on the surface of hematopoietic and non-  
76 hematopoietic cells. It is a key player in the trafficking of lymphocytes and  
77 monocytes/macrophages and has been implicated in the pathophysiology of multiple  
78 diseases, including viral infections and complex disorders with an inflammatory  
79 component (Brelot & Chakrabarti, 2018; Flanagan, 2014; Vangelista & Vento, 2017). In  
80 addition, the CCL5/CCR5 axis represents a major marker of tumor development  
81 (Aldinucci et al., 2020). CCR5 binds several chemokines, including CCL3, CCL4, and  
82 CCL5. Binding of chemokines results in conformational change of the receptor, which  
83 then activates intracellular signaling pathways and leads to cell migration (Flanagan,  
84 2014). CCR5 also binds the envelope glycoprotein of HIV-1, then acting as the major  
85 HIV-1 entry co-receptor (Alkhatib et al., 1996; Brelot & Chakrabarti, 2018). One CCR5  
86 allosteric ligand, maraviroc (MVC), is part of the anti-HIV-1 therapeutic arsenal (Dorr et  
87 al., 2005), although emergence of MVC-resistant variants has been identified in some  
88 patients (Tilton et al., 2010).

89 We and others showed the existence of various CCR5 populations present at the cell  
90 surface (Abrol et al., 2014; Berro et al., 2011; Colin et al., 2013; Colin et al., 2018; Fox et  
91 al., 2015; Jacquemard et al., 2021; Jin et al., 2014; Jin et al., 2018; Scurci et al., 2021).  
92 Computational analysis predicts that CCR5 can adopt an ensemble of low-energy  
93 conformations, each of which being differentially favored by distinct ligands and receptor  
94 mutations (Abrol et al., 2014). CCR5 conformations display distinct antigenic properties,  
95 which vary depending on cell types (Colin et al., 2018; Fox et al., 2015). The multiple  
96 conformations interact differently with distinct ligands (agonist, antagonist, HIV-1  
97 envelope glycoprotein) and differ in their biological properties, HIV co-receptor functions,

98 and abilities to serve as therapeutic targets (Abrol et al., 2014; Colin et al., 2013; Colin et  
99 al., 2018; Jacquemard et al., 2021; Jin et al., 2014; Jin et al., 2018; Scurci et al., 2021).  
100 In particular, coupling to G proteins distinguishes CCR5 populations that are differently  
101 engaged by chemokines and HIV-1 envelope. This explains why HIV-1 escapes  
102 inhibition by chemokines (Colin et al., 2013). In this context, the improved capacity of  
103 chemokine analogs to inhibit HIV infection, as compared to native chemokines, is related  
104 to their ability to target a large amount of CCR5 conformations (Jin et al., 2014).

105 Like other receptors of this class, CCR5 forms homo- and hetero-dimers with other  
106 receptors, which contribute to the diversity of conformational states (Jin et al., 2018;  
107 Sohy et al., 2009). We identified three homo-dimeric organizations of CCR5 involving  
108 residues of transmembrane domain 5 (TM5) (Jin et al., 2018). Two dimeric states  
109 corresponded to unliganded receptors, whereas binding of the inverse agonist MVC  
110 stabilized a third state (Jin et al., 2018). CCR5 dimerization occurs in the endoplasmic  
111 reticulum, thereby regulating the receptor targeting to the cell surface (Jin et al., 2018).  
112 CCR5 dimerization also modulates ligand binding and HIV-1 entry into cells (Colin et al.,  
113 2018). MVC stabilizes CCR5 homodimerization, illustrating that CCR5 dimerization can  
114 be modulated by ligands (Jin et al., 2018), a feature shared with other chemokine  
115 receptors (Isbilir et al., 2020). Allosteric interaction within CCR2/CCR5 heterodimers is  
116 reported as well as cross-inhibition by specific antagonists (Sohy et al., 2009). This  
117 suggests that dimerization impacts therapeutic targeting.

118 To characterize the diversity of CCR5 subpopulations at the cell surface and to  
119 investigate the impact of CCR5 dynamics on its function, we tracked CCR5 fluorescent  
120 particles by total internal reflection fluorescence (TIRF) microscopy (Calebiro et al.,  
121 2013) and quantitatively classify their motion over time using an original statistical  
122 method. We described CCR5 mobility patterns both at the basal state and after ligand

123 binding (using two agonists, the inverse agonist MVC, and HIV-1 envelope  
124 glycoproteins) and under conditions that modulate CCR5 / G protein coupling,  $\beta$ -arrestin  
125 binding, and dimerization. This study provides novel insights into the organization of a  
126 GPCR at the cell surface and the mechanisms regulating its signaling and fate after  
127 activation.

## 128 **Results**

### 129 **Statistical classification of receptor trajectories at the cell membrane**

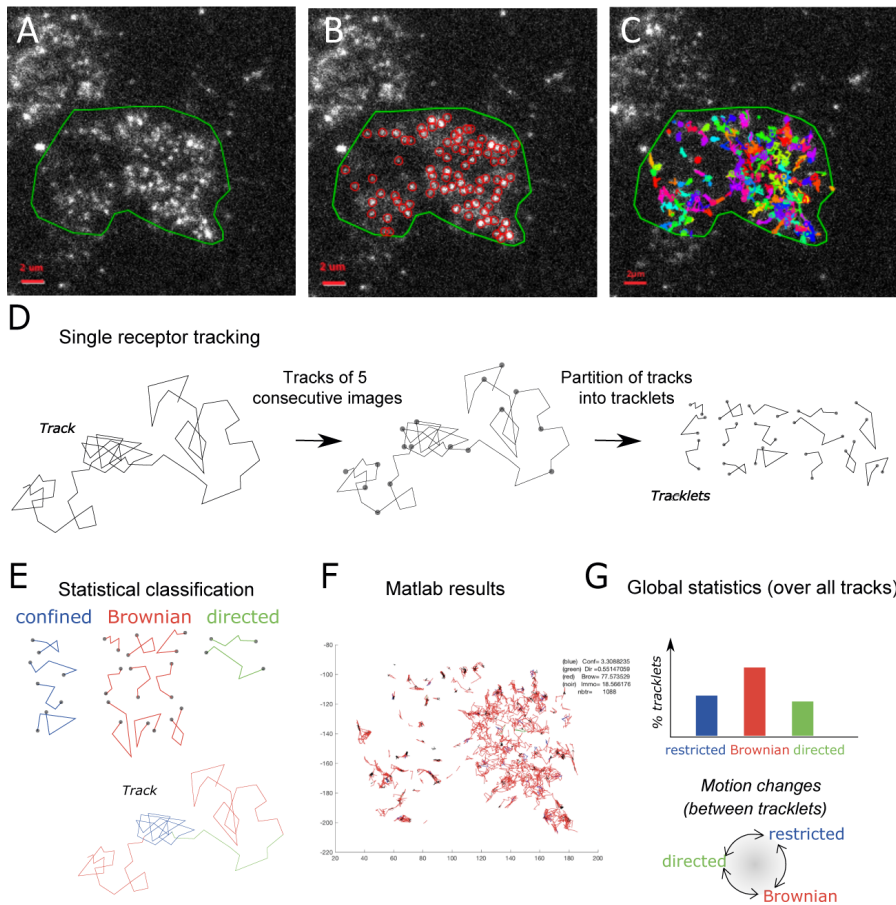
130 We generated a HEK 293 cell line stably expressing a low density of eGFP-CCR5 at the  
131 cell surface ( $< 0.5$  particles/ $\mu\text{m}^2$ ), which is critical for single particle tracking on the  
132 surface of living cells (Calebiro et al., 2013). We choose HEK 293 cells because they do  
133 not express CCR5. Fusion of eGFP to the N-terminus of CCR5 does not alter cell  
134 surface expression of the receptor or its intracellular trafficking (Boncompain et al.,  
135 2019).

136 To study the dynamics of CCR5 as a single particle at the plasma membrane of living  
137 cells, we used TIRF microscopy, which restricts the observation to the first 200 nm from  
138 the coverslip. The acquisitions were carried out at 37 °C with a frequency of 30 Hz (1  
139 image / 33 ms). From the movies obtained, we tracked the motion of the particles over  
140 time using the *Spot tracking* plugin of the ICY software (Chenouard et al., 2013; de  
141 Chaumont et al., 2012) (**Figure 1A-C, Videos 1, 2, 3**, see Material and Methods).

142 The method generally used to evaluate the dynamics of a particle is based on Mean  
143 Square Displacement (MSD) analysis (Qian et al., 1991). However, MSD is a global  
144 analysis of particle trajectory that does not handle possible changes in particle motion. In  
145 particular, it indicates whether the observed motion is standard Brownian motion and  
146 computes the related diffusion coefficient of the trajectory, but it cannot characterize

147 more complex stochastic motions as the frequency of motion changes. In addition, the  
148 MSD analysis does not provide a statistical significance of classified motion. To robustly  
149 characterize the complex stochastic motions of single receptors at the cell membrane,  
150 we used an alternative statistical method. We first partitioned single receptor trajectories  
151 into small tracklets (with  $N = 5$  consecutive detections each) to mitigate the risk of  
152 tracking errors over long trajectories, and to detect potential motion changes between  
153 tracklets within each single receptor trajectory (**Figure 1D**). We first evaluated immobile  
154 objects and then used a robust statistical method to classify tracklet motion (see Material  
155 and Methods and **Figure 1E-F**). Briefly, for each tracklet  $X$ , we computed the statistics  
156  $S(X, N)$  introduced in (Briane et al., 2018) that evaluate the ratio between the maximal  
157 distance reached by the tracklet particle from the initial point and the motion standard  
158 deviation. We then used the statistics  $S(X, N)$  to classify each tracklet into one of the  
159 three following motion categories: *confined*, *Brownian*, or *directed* stochastic motion. For  
160 this, we computed  $S(X, N)$  for each tracklet and compared it to the quantiles  $(q_\alpha, q_{1-\alpha})$ ,  
161 which are statistical reference values of Brownian motion at level  $\alpha$  and  $(1 - \alpha)$ .  
162 Quantiles of  $S(X, N)$  only depend on  $N$  and  $\alpha$  (Briane et al., 2018), and can be evaluated  
163 independently of the characteristics of experimental trajectories. Finally, tracklets  $X$  were  
164 classified according to the associated stochastic motion: confined (if  $S(X, N) < q(\alpha)$ ),  
165 Brownian (if  $q(\alpha) \leq S(X, N) < q(1 - \alpha)$ ), and directed motion (if  $q(1 - \alpha) \leq S(X, N)$ )  
166 (**Figure 1-figure supplement 1**). We used this statistical classification procedure, with  
167  $\alpha = 0.05$ , to characterize the dynamics of CCR5 particles at the cell membrane.





168

169 **Figure 1.** Single particle detection of eGFP-CCR5 using TIRF microscopy and analysis with the  
 170 statistical method. (A) Distribution of eGFP-CCR5 stably expressed in HEK 293 cells. Imaging  
 171 was acquired at 30 Hz. The region of interest defined by the green line is used for A-C and F.  
 172 Analysis of movies was performed using the ICY software and (B) the *Spot detection* and (C) the  
 173 *Spot tracking* pluggins. Scale bare 2  $\mu\text{m}$ . (D) Single receptor tracks were partitionned into  
 174 tracklets of 5 images each. (E) Analysis of tracks with the statistical method: tracklets were  
 175 classified into confined, Brownian, and directed motion. (F) Results obtained from Matlab. (G)  
 176 Pooled tracklets classification provided a global estimate of receptor dynamics and the number of  
 177 motion changes along the track (transition rates). (Restricted motions: immobile and confined  
 178 motions).

179 **Video 1.** TIRF movie of a cell stably expressing eGFP-CCR5-WT acquired at 30 Hz. The region  
 180 of interest was defined by the green line.

181 **Video 2.** TIRF movie of the same cell as in video 1 analyzed using the Icy software. Red circles  
 182 correspond to the detection of bright spots using the *Spot detection* pluggin.

183 **Video 3.** TIRF movie of the same cell as in video 1 and 2 analyzed using the Icy software and the  
 184 *Spot tracking* pluggin. Colored lines correspond to the tracked spots.

185 **Figure supplement 1.** Validation of the statistical method using simulated trajectories.

186 **CCR5 particles have different motions at the plasma membrane**

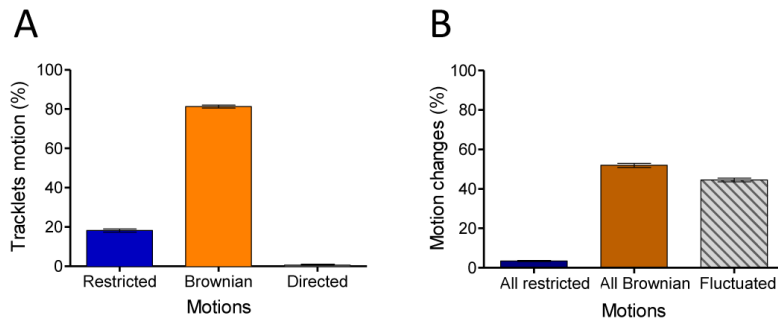
187 We investigated CCR5 mobility in the basal state using the statistical method described  
188 above (**Figure 1**). The result of the classification of all the pooled tracklets provided a  
189 global estimate of the receptor dynamics, while the number of motion changes along the  
190 same trajectory gave us an estimate of the overall stability of the motion (**Figure 1G**).

191 In the basal state, the eGFP-CCR5 particles distributed homogeneously over the entire  
192 membrane surface (**Figure 1A, Videos 1, 2, 3**). However, the motions of eGFP-CCR5  
193 particles were heterogeneous (**Figure 2A**). Eighty percent of the pooled CCR5 tracklets  
194 were mobile with Brownian motion, while 20 % were classified as restricted motion (i.e.  
195 immobile and confined) (**Figure 2A**). We observed almost no directed trajectories (< 0.5  
196 %). Around fifty percent of particles (52 %) exhibited Brownian motion over the entire  
197 length of the path (**Figure 2B**). The other half fluctuated between Brownian and  
198 restricted motion (**Figure 2B**). This high degree of fluctuation between motions within  
199 one trajectory suggested the existence of transient conformations of CCR5 at the  
200 plasma membrane.

201 Together, these analyses revealed heterogeneity of CCR5 motion at the basal state  
202 consistent with the diversity of CCR5 forms described previously by other methods  
203 (Abrol et al., 2014; Colin et al., 2013; Fox et al., 2015; Jin et al., 2018; Scurci et al.,  
204 2021).

205

206



207

208 **Figure 2.** In the basal state, CCR5 exhibits different motions at the plasma membrane. (A)  
209 Distribution of tracklets motion: restricted, Brownian, or directed (mean  $\pm$  SEM, n= 28 305 tracks  
210 from 19 cells, 3 independent experiments). (B) Distribution of tracklets motion changes along  
211 tracks (mean  $\pm$  SEM, n= 48 237 tracks from 45 cells, 7 experiments).

212

### 213 **Multiple ligands impact CCR5 mobility differently**

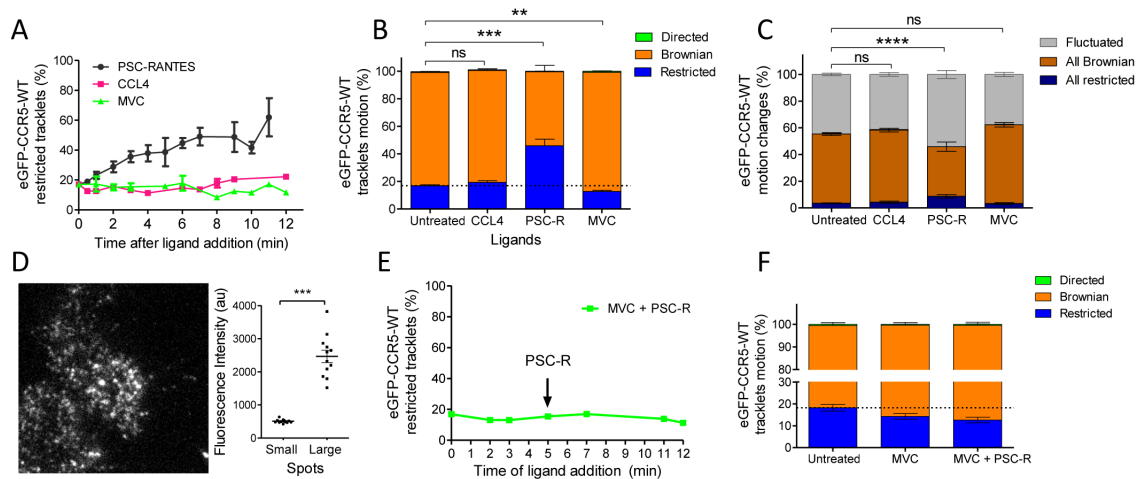
214 Since ligands modulate the conformation of CCR5 (Colin et al., 2018; Jacquemard et al.,  
215 2021; Jin et al., 2018), we investigated the impact of ligand binding on its spatiotemporal  
216 dynamic properties. We evaluated the effect of saturating concentration of ligands (two  
217 agonists with different efficacies and the inverse agonist MVC, i.e. a ligand with a  
218 negative efficacy) on CCR5 trajectories at the plasma membrane over time. We first  
219 incubated the cells in the presence of the native chemokine CCL4 at a saturating  
220 concentration ( $> 100$  nM,  $k_d = 0.4$  nM) (Colin et al., 2013) for the indicated time. The  
221 mobility of the receptor was then assessed immediately after addition of the ligand in a  
222 window of 1 to 12 min (**Figure 3A**). CCL4 triggered no significant change in CCR5  
223 mobility after 10 min of stimulation (**Figure 3B**). However, a longer time of CCL4  
224 stimulation ( $> 12$  min) increased the percentage of restricted CCR5 tracklets, indicating  
225 localized immobility of a small fraction of receptors (**Figure 3-figure supplement 1**). We  
226 also noted the formation of large and immobile spots after 12 min of stimulation (**Video**  
227 **4**).

10

228 We compared the effect of CCL4 with that of an agonist targeting a greater proportion of  
229 receptor conformations and displaying a greater agonist efficacy, PSC-RANTES (Escola  
230 et al., 2010; Jin et al., 2014). We incubated the cells in the presence of a saturating  
231 concentration of PSC-RANTES (20 nM,  $K_i = 1.9$  nM) (Colin et al., 2013) and evaluated  
232 the motion of the receptors under the same conditions. PSC-RANTES triggered a  
233 progressive increase in the number of tracklets classified as restricted motion over time  
234 (**Figure 3A**). Ten minutes after stimulation with PSC-RANTES, about 50 % of eGFP-  
235 CCR5 tracklets were in a restricted state (46 %) against 17 % under basal conditions  
236 (**Figure 3B**). Consequently, the fraction of all Brownian trajectories decreased, while the  
237 fraction of fluctuated and all restricted trajectories increased (**Figure 3C**).  
238 Simultaneously, we observed the formation of large immobile spots (5 to 10 per cell) in  
239 PSC-RANTES-treated cells (**Figure 3D, left**). These large spots had a long lifespan (50  
240 to 100 frames) (**Video 5**). The quantification of the fluorescence intensity of the spots  
241 from the frame 1 of live-imaging movies showed that the large spots had, on average,  
242 intensity 4 times higher than the other spots, indicating a clustering of at least 4  
243 receptors per large spot (**Figure 3D, right**). These results revealed a change in CCR5  
244 mobility upon activation towards receptor immobilization and clustering, supporting  
245 receptors trapping in nanodomains.

246 Unlike agonists, the inverse agonist MVC (10  $\mu$ M,  $K_d = 1$  nM) did not restrict receptor  
247 mobility (**Figure 3A, B, C**). On the contrary, the fraction of restricted eGFP-CCR5  
248 tracklets at the surface of MVC-treated cells showed a slight decrease compared to  
249 untreated cells (**Figure 3B**). We verified the specificity of PSC-RANTES-induced CCR5  
250 immobility by treating cells with MVC before PSC-RANTES stimulation. MVC treatment  
251 impaired PSC-RANTES-induced receptor immobilization (**Figure 3E-F**), indicating that  
252 CCR5 immobilization depended on PSC-RANTES binding to CCR5.

253 These results showed that distinct ligands differently stabilize CCR5 in living cells, in  
 254 accordance with our previous results (Colin et al., 2013; Colin et al., 2018; Jin et al.,  
 255 2014; Jin et al., 2018). Interestingly, the amount of receptors immobilized correlates with  
 256 the efficacy of ligands (PSC-RANTES > CCL4 > MVC), suggesting a link between  
 257 receptor activation and immobilization.  
 258



259

260 **Figure 3.** Different ligands, agonists and inverse agonist, impact CCR5 mobility differently. eGFP-  
 261 CCR5-WT expressing cells were treated or not with a saturating concentration of agonists (CCL4,  
 262 200 nM or PSC-RANTES, 20 nM) or inverse agonist (maraviroc, 10  $\mu$ M) and single particle  
 263 tracking analysis was performed. (A) Percentage of restricted tracklets after treatment over time  
 264 (n= tracks from 10, 4, and 3 cells for PSC-RANTES, CCL4, and MVC conditions respectively, at  
 265 least 3 independent experiments). (B) Distribution of tracklets motion after 10 min of treatment  
 266 (mean  $\pm$  SEM, n= 40 564, 15 421, 11 213, 9 828 tracks for each condition from 38, 14, 12, 9 cells  
 267 respectively, at least 3 independent experiments). Unpaired t test on restricted motions only: ns,  
 268 nonsignificant; \*\* $P \leq 0.005$ ; \*\*\* $P \leq 0.0001$ . (C) Distribution of tracklets motion changes along  
 269 tracks after 10 min of treatment (mean  $\pm$  SEM, n= 48 237, 8 954, 16 668, 9 828 tracks from 45, 9,  
 270 17, 9 cells for each condition, at least 3 experiments). Unpaired t test on all restricted motions  
 271 only: ns, nonsignificant; \*\*\*\* $P \leq 0.0001$ . (D) (Left) Single particle detection of eGFP-CCR5-WT  
 272 after 3 min of stimulation with PSC-RANTES (20 nM) from frame 1 of live-imaging movie (one  
 273 representative image). (Right) Mean of the sum of fluorescence intensity under large immobile  
 274 spots and small mobile spots after 3 to 10 min of stimulation (mean  $\pm$  SEM, n= at least 40 spots  
 275 from 12 cells, 3 experiments). (E) Percentage of restricted tracklets after successive stimulation

276 with maraviroc (10  $\mu$ M, 5 min) and PSC-RANTES (20 nM, 5 to 12 min) (one representative  
277 experiment). (F) Distribution of tracklets motions after successive stimulation with maraviroc (10  
278  $\mu$ M, during 5 min) and PSC-RANTES (20 nM, during 6 min) (mean  $\pm$  SEM, n= 14 467, 3 601, 2  
279 075 tracks from 14, 2, 2 cells respectively, 1 experiment).

280 **Figure supplement 1.** Effect of CCL4 on CCR5 mobility.

281 **Video 4.** TIRF movie acquired at 30 Hz of a cell stably expressing eGFP-CCR5-WT and treated  
282 by CCL4 (100 nM) for 14 min.

283 **Video 5.** TIRF movie acquired at 30 Hz of cells stably expressing eGFP-CCR5-WT and treated  
284 by PSC-RANTES (20 nM) for 3 min.

285

### 286 **Gi coupling and $\beta$ -arrestin association influence CCR5 motion differently under basal state** 287 **and stimulated conditions**

288 To further address the above hypothesis, we sought to determine whether the mobility of  
289 CCR5 is influenced by its coupling to Gi protein, which stabilizes the receptor in an  
290 activated state. We analyzed the pool of restricted CCR5 tracklets in the presence of  
291 pertussis toxin (PTX), which uncouples the receptor from Gi proteins (**Figure 4A**).

292 In the basal state, the fraction of restricted eGFP-CCR5 tracklets from cells pre-treated  
293 with PTX decreased compared to untreated cells (**Figure 4A**). Under this condition, PTX  
294 also inhibited chemotaxis, a process that depends on CCR5 coupling to Gi proteins  
295 (**Figure 4-figure supplement 1**). These results thus suggested that a small subset of  
296 CCR5 is in a Gi protein-bound form in its basal state, which may contribute to the  
297 transient restriction of the motion of CCR5 at the cell surface.

298 After stimulation, receptor immobilization could be due to the recruitment of receptors in  
299 hub areas where the receptor meets the activation machinery and in particular the G  
300 protein (Sungkaworn et al., 2017). To evaluate the role of Gi coupling on receptor  
301 immobilization after PSC-RANTES stimulation, we analyzed tracks of TIRF movies of  
302 PSC-RANTES-stimulated cells pretreated or not with PTX. In this condition, the fraction  
303 of restricted tracklets increased over time after stimulation in the same proportion

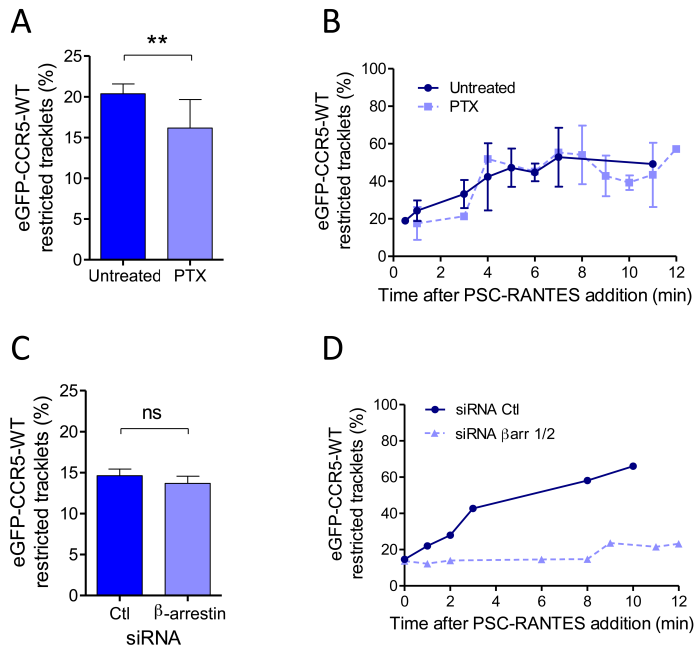
304 regardless of PTX treatment (**Figure 4B**). This suggested that Gi coupling was not  
305 involved in PSC-RANTES dependent immobilization of CCR5 after several minutes of  
306 stimulation. This result is actually consistent with our previous study showing high affinity  
307 interaction of PSC-RANTES with Gi protein uncoupled CCR5 (Colin et al., 2013).

308 After stimulation by PSC-RANTES, CCR5 follows a clathrin-dependent endocytosis  
309 pathway, involving  $\beta$ -arrestins, which bridge the receptor to AP2 and clathrin (Delhaye et  
310 al., 2007; Jin et al., 2014). We previously showed that silencing  $\beta$ -arrestin 1 and  $\beta$ -  
311 arrestin 2 endogeneous expressions with siRNA decreased CCR5 internalization after  
312 PSC-RANTES stimulation (Jin et al., 2014). Silencing  $\beta$ -arrestins in eGFP-CCR5 cells  
313 with siRNA did not impact eGFP-CCR5 motion in the basal state (**Figure 4C**) but  
314 inhibited PSC-RANTES-induced eGFP-CCR5 immobilization and clustering (**Figure 4D**).

315 These experiments indicated that  $\beta$ -arrestins contributed to CCR5 immobilization after  
316 stimulation.

317 Together, these results pointed to the existence of a fraction of CCR5 in a transient pre-  
318 assembled signaling complex in the basal state, which is consistent with previous  
319 studies showing CCR5 constitutive activity (Garcia-Perez et al., 2011; Lagane et al.,  
320 2005). They also suggested that the fate of CCR5 several minutes after activation is  
321 independent of Gi coupling but dependent on  $\beta$ -arrestin recruitment, in accordance with  
322 receptor desensitization and uncoupling after activation (Flanagan, 2014).





323

324 **Figure 4.** Gi coupling and  $\beta$ -arrestins association restrict CCR5 mobility at basal state or after  
 325 PSC-RANTES stimulation. (A) Percentage of restricted tracklets in eGFP-CCR5-WT expressing  
 326 HEK 293 cells pre-treated or not with 100 ng/ml of PTX for 3 h (mean  $\pm$  SEM, n= 8 614 and 11  
 327 377 tracks for each condition, 12 and 15 cells respectively, 3 independent experiments). Unpaired  
 328 t test: p value 0.0083\*\*. (B) Percentage of restricted tracklets over time of eGFP-CCR5-WT  
 329 expressed on PSC-RANTES (20 nM) treated cells after incubation or not with PTX (100 ng/ml)  
 330 (mean  $\pm$  SD, n= 3 independent experiments). (C) Proportion of restricted tracklets in eGFP-  
 331 CCR5-WT expressing cells transfected with siRNA  $\beta$ arr1/2 (mean  $\pm$  SD, n= 6 754 and 8 854  
 332 tracks for each condition, from 7 and 8 cells respectively). Unpaired t test: p value 0.46, ns. (D)  
 333 Percentage of restricted tracklets over time of eGFP-CCR5-WT expressed on PSC-RANTES (20  
 334 nM) treated cells after siRNA  $\beta$ arr 1/2 transfection (n= 1 representative experiment).

335 **Figure supplement 1.** Effect of PTX treatment on chemokine-mediated chemotaxis.

336

### 337 **Immobilization of CCR5 after stimulation depends on its oligomeric state**

338 We previously showed by energy transfer experiments that a point mutation of CCR5 in  
 339 TM5 (L196K) leads to a receptor, which has a reduced dimerization capacity compared  
 340 to CCR5-WT (Jin et al., 2018). To study the role of CCR5 dimerization on its mobility, we



341 generated HEK 293 cells stably expressing eGFP-CCR5-L196K in the same proportion  
342 to the clone expressing eGFP-CCR5-WT.

343 We studied the molecular composition of both eGFP-CCR5-L196K and eGFP-CCR5-WT  
344 in these cells by analyzing the fluorescence intensity of eGFP per spot from the frame 1  
345 of live-imaging movies. In a previous study, we calibrated the fluorescence intensity of  
346 eGFP while spotted on glass coverslip (Salavessa et al., 2021). We showed that most of  
347 eGFP spots bleached in a single step, suggesting that eGFP corresponds to 1 molecule,  
348 with an average fluorescence intensity of 300-500 au (Salavessa et al., 2021). In eGFP-  
349 CCR5 expressing cells, the fluorescence intensities were distributed in Gaussians, which  
350 we classified with the Akaike information criterion (AIC, see Material and Methods)  
351 (Akaike, 1974). We observed three types of Gaussians with double or triple mean  
352 intensities (300, 600, 900 au), which likely correspond to spots comprising 1, 2, or 3  
353 receptors (**Figure 5A**). This reflected the existence of a heterogeneous distribution of  
354 receptors. In this classification, the WT receptor distributed in 50 % monomers, 40 %  
355 dimers, and 10 % oligomers (trimers or more) at the plasma membrane, while eGFP-  
356 CCR5-L196K was mostly in a monomeric form (75 % monomers, 25 % dimers) (**Figure**  
357 **5B**). These results revealed that eGFP-CCR5-L196K was mostly monomeric at the  
358 surface of living cells and that the fusion of eGFP to CCR5 did not alter the effect of  
359 L196K mutation on CCR5 dimerization.

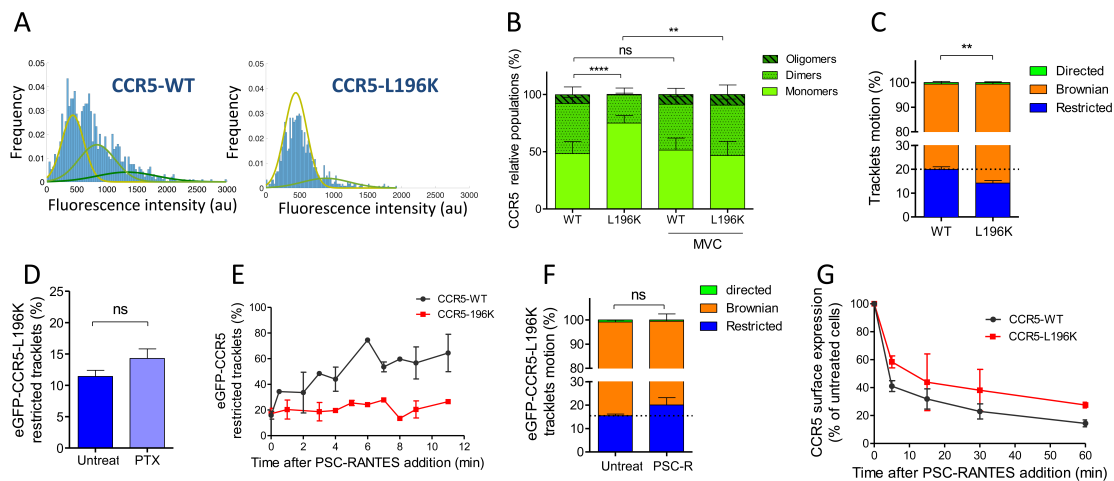
360 In the presence of MVC, both eGFP-CCR5-WT and eGFP-CCR5-L196K distribution  
361 exhibited 50 % monomers, 40 % dimers, and 10 % oligomers (**Figure 5B**). The change  
362 of eGFP-CCR5-L196K stoichiometry distribution in the presence of MVC confirmed our  
363 previous results showing that MVC stabilized CCR5 in a novel dimeric form, which was  
364 not disrupted by the introduction of a lysine in TM5 (Jin et al., 2018).

365 To investigate the impact of CCR5 dimerization on its mobility, we compared the motion  
366 of eGFP-CCR5-L196K to eGFP-CCR5-WT at the cell surface. As for eGFP-CCR5-WT,  
367 eGFP-CCR5-L196K tracklets were predominantly classified as Brownian tracklets  
368 motion (85 % of the tracklet motions are Brownian), suggesting that monomeric and  
369 dimeric forms of CCR5 exhibited similar behavior at the surface of cells in the basal state  
370 (**Figure 5C**). However, we observed a decrease in the proportion of restricted tracklets  
371 for eGFP-CCR5-L196K compared to eGFP-CCR5-WT (**Figure 5C**). These data  
372 suggested that dimerization contributed to the stability of CCR5 molecules at the cell  
373 surface, as previously proposed (Calebiro et al., 2013).

374 To test whether eGFP-CCR5-L196K coupling to Gi protein accounts in its restriction as  
375 shown for eGFP-CCR5-WT, we pre-treated cells with PTX. Contrary to eGFP-CCR5-  
376 WT, PTX treatment did not alter the proportion of the eGFP-CCR5-L196K restricted  
377 tracklets pool (**Figure 5D**), suggesting that most of eGFP-CCR5-L196K were not  
378 precoupled to the Gi protein at the basal state or that G protein precoupling induces  
379 differential effects on the dynamics of both receptors. Supporting the first hypothesis,  
380 previous biochemical and energy transfer experiments on a distinct GPCR showed that  
381 there could be a link between dimerization and Gi coupling at basal state (Maurice et al.,  
382 2010).

383 To investigate whether dimerization affected CCR5 mobility after stimulation, we  
384 analyzed single-molecule movies of eGFP-CCR5-L196K cells after PSC-RANTES  
385 treatment (**Figure 5E-F**). Contrary to eGFP-CCR5-WT massive immobilization and  
386 clustering upon PSC-RANTES treatment (**Figure 3A-B**), eGFP-CCR5-L196K was only  
387 slightly immobilized after 10 minutes of treatment (**Figure 5E-F**), while large immobile  
388 spots were not detected (**Video 6**). This result indicated that CCR5 immobilization and  
389 clustering after stimulation depend on CCR5 dimerization.

390 Because CCR5-WT immobilization involved  $\beta$ -arrestins (**Figure 4D**), an explanation for  
 391 the lack of PSC-RANTES induced eGFP-CCR5-L196K immobilization is that eGFP-  
 392 CCR5-L196K fails to recruit  $\beta$ -arrestins and therefore, is not desensitized and/or  
 393 internalized after stimulation. To test this hypothesis, we evaluated PSC-RANTES-  
 394 induced internalization of the dimerization-compromised mutant compared to the WT  
 395 receptor in feeding experiments using FLAG-SNAP-CCR5 expressing cells (Delhaye et  
 396 al., 2007; Jin et al., 2018). A saturating concentration of PSC-RANTES decreased cell  
 397 surface expression of both receptors, but not in the same proportion (**Figure 5G**),  
 398 suggesting that CCR5 dimerization impacted its internalization process. However, while  
 399 eGFP-CCR5-L196K immobilization was drastically impaired, its internalization was not  
 400 fully abrogated. These results supported that dimerization is a pre-requisite to the  
 401 immobilization of the receptor, but was not essential for receptor internalization. This  
 402 ruled out a necessary step of massive receptor immobilization before internalization and  
 403 revealed that different mechanisms may contribute to CCR5 internalization depending  
 404 on the receptor conformation.



405

406 **Figure 5.** Dimerization through TM5 alters CCR5 mobility and trafficking. (A) Distribution of the  
 407 fluorescence intensity of spots detected at the surface of HEK 293 cells expressing eGFP-CCR5-

408 WT or eGFP-CCR5-L196K. One representative experiment out of 6 (n= 943 spots from 6 cells  
409 and 1 207 spots from 8 cells for each condition); (B) Quantification of the fluorescent populations  
410 depending on the mean of the gaussian at the surface of cells treated or not with MVC (10  $\mu$ M)  
411 (mean  $\pm$  SD, nWT = 5 171 spots from 47 cells, 9 experiments; nL196K = 3 144 spots from 30  
412 cells, 5 experiments; nWT-MVC = 3 055 spots from 25 cells, 4 experiments; nL196K-MVC = 1  
413 776 spots from 16 cells, 3 experiments). Unpaired t test on monomers: p value  $**P \leq 0.005$ ;  $****P$   
414  $\leq 0.0001$ ; ns  $P \geq 0.05$ ; (C) Distribution of pooled tracklets motion of eGFP-CCR5-WT and eGFP-  
415 CCR5-L196K (mean  $\pm$  SEM, n = 11 321 tracks from 10 cells and 10 460 tracks from 12 cells in  
416 each condition; 2 independent experiments). Unpaired t test on the restricted tracklets: p value  
417 0.0015\*\*. (D) Percentage of restricted tracklets in eGFP-CCR5-L196K cells pre-treated or not  
418 with 100 ng/ml of PTX for 3 h (mean  $\pm$  SEM, n= 7 cells). Unpaired t test: p value 0.15, ns. (E)  
419 Percentage of restricted tracklets over time of PSC-RANTES induced eGFP-CCR5-WT or eGFP-  
420 CCR5-L196K expressing cells (mean  $\pm$  SD of 3 independent experiments). (F) Distribution of  
421 tracklets motion after 10 min of PSC-RANTES stimulation (20 nM) (mean  $\pm$  SEM, n= 11 218  
422 tracks from 10 cells and 5 433 tracks from 4 cells for untreated and PSC-RANTES treated cells  
423 respectively, 2 independent experiments). Unpaired t test: p value 0.055, ns. (G) CCR5  
424 internalization. Cell surface expression of FLAG-SNAP-CCR5-WT or FLAG-SNAP-CCR5-L196K  
425 was monitored by flow cytometry in stable HEK 293 cell clones after stimulation with a saturating  
426 concentration of PSC-RANTES (20 nM) for the indicated time. The percentage of total bound  
427 anti-FLAG antibody was calculated from the mean fluorescence intensity relative to untreated  
428 cells (mean  $\pm$  SD from two independent experiments).

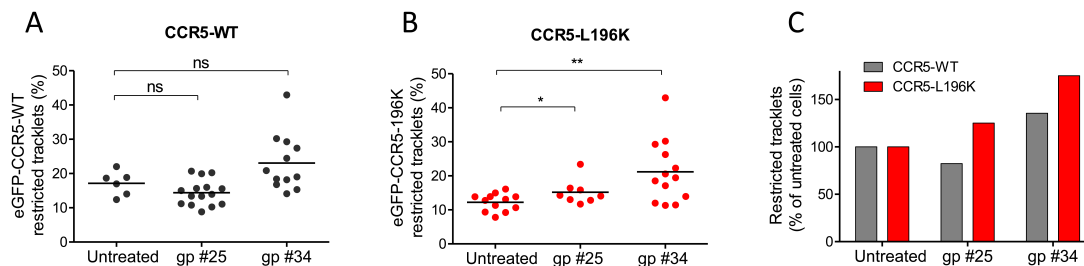
429 **Video 6.** TIRF movie acquired at 30 Hz of a cell stably expressing eGFP-CCR5-L196K and  
430 treated by PSC-RANTES (20 nM) for 2 min.

431

### 432 **Distinct HIV-1 envelope glycoproteins gp120 differently influenced CCR5 dynamics**

433 Pharmacological studies suggested that distinct CCR5 conformations at the cell surface  
434 differentially engaged distinct HIV-1 envelope glycoproteins gp120 (Colin et al., 2018).  
435 Since we showed here that CCR5 mobility and ligand engagement are intrinsically  
436 linked, we used our mobility classification method to characterize the effect of different  
437 HIV-1 gp120s on CCR5 mobility and tested in living cells whether different gp120s  
438 engaged different conformational states of CCR5.

439 We tested the effect of two soluble gp120s, gp #25 and gp #34, described to induce  
440 distinct conformational rearrangements in CCR5 (Jacquemard et al., 2021), and to have  
441 different binding capacities to the receptor and fusogenic efficacies (Colin et al., 2018).  
442 Twenty min of gp120s exposure slightly modulated the mobility of eGFP-CCR5-WT,  
443 although this trend was not statistically significant (**Figure 6A, C**). However, and in  
444 contrast to what we observed using chemokines as ligands, the HIV-1 gp120s  
445 immobilized eGFP-CCR5-L196K, with gp #34 having the highest effect (**Figure 6B, C**).  
446 This suggested (i) that gp120s stabilized CCR5 conformations, which were different from  
447 those stabilized by chemokines, and (ii) that different envelopes also stabilized  
448 differently CCR5 conformations, in accordance with our previous result (Colin et al.,  
449 2013; Colin et al., 2018).  
450



451

452 **Figure 6.** HIV-1 gp120s binding restricts CCR5 mobility. Soluble gp120s were incubated 30 min  
453 at RT in the presence of soluble CD4 (ratio sCD4/gp120 >5) to allow their binding to CCR5. Then,  
454 gp120-sCD4 complexes were added to live eGFP-CCR5-WT or eGFP-CCR5-L196K expressing  
455 cells during at least 20 min before single particle analysis. The proportion of restricted tracklets  
456 after gp #25 and gp #34 treatment (100 nM) (in complex with sCD4) on eGFP-CCR5-WT (A, C)  
457 or eGFP-CCR5-L196K (B, C) expressing cells was represented (n=3 independent experiments).  
458 Unpaired t test: \*\* $P \leq 0.005$ ; \*\*\* $P \leq 0.0001$ ; ns  $P \geq 0.05$ .

459

## 460 **Discussion**

461

462 In this study, we developed a statistical method to classify the motion of fluorescent  
463 particles at the cell surface. We applied this method to track eGFP-CCR5 under different  
464 stimuli and different conformations. We showed that the receptor fluctuates between  
465 Brownian and restricted motions at the cell surface, depending on (1) precoupling to Gi  
466 proteins at the basal state; (2) the type of ligand bound to the receptor, and in particular  
467 its efficacy on receptor activation and interaction with  $\beta$ -arrestins; and (3) receptor  
468 dimerization. Indeed, CCR5 mobility changes following agonist stimulation were  
469 dependent on  $\beta$ -arrestins recruitment and receptor dimerization, but were independent of  
470 receptor interaction with Gi proteins. This study demonstrated that coupling single  
471 molecule tracking to a statistical classification of trajectories is a powerful approach to  
472 characterize the dynamic behaviors of functionally different receptor populations at the  
473 plasma membrane.

### 474 **Diversity of ligand-free forms of CCR5 at the cell surface.**

475 Quantitative analysis of the motion of CCR5 particles and their numbering within the  
476 fluorescent spots present at the cell membrane of HEK 293 cells revealed in the basal  
477 state (i) two classes of receptor trajectories, Brownian (80 %) and restricted (20 %)  
478 (**Figure 2**) and (ii) different oligomeric states (**Figure 5**): monomers (50 %), dimers (40  
479 %), and oligomers (more than three receptors) (10 %). These features shared with other  
480 GPCRs (Gormal et al., 2020; Martinez-Munoz et al., 2018; Sungkaworn et al., 2017;  
481 Tabor et al., 2016; Veya et al., 2015), established the existence of multiple CCR5 forms  
482 at the cell membrane.

483 In addition, our statistical method highlighted a fluctuation between Brownian and  
484 restricted states during the same trajectory, suggesting the existence of transient  
485 populations of receptors (**Figure 2B**). The change in mobility between periods of

486 confinement separated by free diffusion could be attributed to the molecular organization  
487 of the receptor oscillating between different oligomeric forms at the cell surface  
488 (monomers, dimers, oligomers), as proposed for CCR5 (Jin et al., 2018) or other  
489 receptors (Isbilir et al., 2020; Kasai et al., 2018; Martinez-Munoz et al., 2018; Tabor et  
490 al., 2016). In agreement with this, we observed differences in mobility between  
491 monomers and dimers of CCR5 (**Figure 5C**). Change in mobility could also be linked to  
492 a transient coupling to G proteins, leading to a transient immobility of the receptor in the  
493 basal state. This hypothesis is supported by our data in the presence of PTX (**Figure**  
494 **4A**) or in the presence of the inverse agonist MVC (**Figure 3A, B**), which both uncouple  
495 the receptor from G proteins and decreased the proportion of immobile receptors. These  
496 data are consistent with dual-color TIRF-M analysis of adrenergic receptor and G  
497 protein, showing that an active receptor-G protein complex is formed in a confined  
498 region of the plasma membrane at the basal state and lasts around 1 second  
499 (Sungkaworn et al., 2017). However, they contrast with a study on mGluR3 showing  
500 higher mobility of the receptor when complexed with G protein (Yanagawa et al., 2018).  
501 This suggested that dynamics of distinct GPCRs can be differently impacted by coupling  
502 to G proteins. Regarding  $\beta$ -arrestin association, we showed using siRNA that CCR5 was  
503 not precoupled to  $\beta$ -arrestins in its basal state (**Figure 4C**). This result suggests that  
504 CCR5 conformations, which bind to G proteins are not recognized by  $\beta$ -arrestins. This is  
505 consistent with the idea that the conformations of receptors interacting with G proteins  
506 and  $\beta$ -arrestins are different (Lagane et al., 2005).

#### 507 **Different ligands recognize/stabilize different sets of CCR5.**

508 We showed that CCR5 mobility is influenced differently according to the ligand it binds.  
509 Chemokine-induced activation of eGFP-CCR5-WT decreased mobility and leads to  
510 clustering (**Figure 3B, D**), effects not observed with the inverse agonist MVC and

511 abolished by MVC (**Figure 3A, B and Figure 3E, F**). This result reinforces the link  
512 between GPCR mobility and ligand binding proposed for GPCRs of different classes  
513 (Gormal et al., 2020; Moller et al., 2020; Veya et al., 2015; Yanagawa et al., 2018).

514 We also showed that two agonists targeting different amount of receptors (CCL4 and  
515 PSC-RANTES) (**Figure 3**) restricted receptor motion in a different proportion, leading to  
516 speculate a relationship between mobility restriction and quantity of targeted receptor,  
517 the greater the number of receptors targeted, the more receptors immobilized and  
518 trapped. Although other possibilities should be considered, such as the dynamic nature  
519 of the ligand-bound conformations, we proposed that characterizing ligands by their  
520 impact on receptor motion opens a new way to classify biased ligands.

521 Applied to viral envelope glycoproteins, our single-particle approach revealed that HIV-1  
522 gp120s displayed an agonist-like influence on CCR5 mobility, albeit to different extent  
523 according to the nature of the gp120 (**Figure 6**). This feature contrasts with the cryo-EM  
524 structure of the CD4-gp120-CCR5 complex, showing that CCR5 adopts inactive  
525 conformation (Shaik et al., 2019). However, it is in line with gp120s-induced CCR5  
526 signaling (Brelot & Chakrabarti, 2018; Flanagan, 2014) and with recent MD simulations  
527 showing that gp120 binding reorients characteristic microswitches involved in GPCR  
528 activation (Jacquemard et al., 2021). The fact that the fraction of immobilized receptors  
529 varied between gp120s could reflect that they do not bind to the same CCR5  
530 conformations, as previously shown (Colin et al., 2018; Jacquemard et al., 2021), and  
531 suggests that these gp120s behave themselves as biased agonists. These features of  
532 gp120s will help understand the determinants of HIV-1 tropism.

533



534 **Single particle tracking analysis revealed that dimerization regulates the fate of activated**  
535 **CCR5.**

536 Our results suggest that receptor dimerization may regulate precoupling of CCR5 to Gi  
537 proteins. Indeed, the mobility of the dimerization-compromized mutant eGFP-CCR5-  
538 L196K was not affected by PTX treatment, in contrast to the WT receptor (**Figure 4A**  
539 **and Figure 5D**). This suggests that most eGFP-CCR5-L196K receptors that reside  
540 preferentially as monomers are not coupled to Gi proteins in the basal state, in  
541 agreement with previous conclusion on CXCR4 (Isbilir et al., 2020). Alternatively, but not  
542 exclusively, CCR5-L196K dimers might also be impaired in their ability to be precoupled  
543 to Gi proteins, contrary to WT receptor dimers.

544 Our analysis suggests that dimerization is a pre-requisite to receptor immobilization and  
545 clustering upon activation by chemokine agonists. Indeed, unlike eGFP-CCR5-WT,  
546 eGFP-CCR5-L196K receptors are only marginally immobilized in the presence of PSC-  
547 RANTES (**Figure 5E**). This result is not due to impaired binding of the chemokine,  
548 because we controlled that PSC-RANTES induced efficient endocytosis of the mutant  
549 receptor (**Figure 5G**). Receptor immobility and clustering were independent of Gi protein  
550 coupling, as exemplified by unaffected CCR5 mobility after 10 min of agonist stimulation  
551 in PTX pre-treated cells (**Figure 4B**), but most likely related to uncoupled and  
552 desensitized form of CCR5 that accumulate in CCS (clathrin-coated structures), as  
553 proposed (Grove et al., 2014; Yanagawa et al., 2018). This hypothesis was strengthened  
554 with the essential role of  $\beta$ -arrestins in activated receptor immobility and clustering  
555 (**Figure 4D**). We cannot rule out that activated receptor clustering may in addition  
556 correspond to an accumulation of receptor in early endosome for a second phase of  
557 activation (Irannejad et al., 2013).

558 In line with this, we showed that dimerization regulates endocytosis (**Figure 5G**). The  
559 lack of immobilization of the dimerization-compromised mutant leads to a suboptimal  
560 internalization of the receptor. This could be due to the impact of dimerization on the  
561 route of endocytosis (dependent or independent of CCS) or on the association of  $\beta$ -  
562 arrestins with the receptor, which stability regulates the fate of the receptor (Bonsch et  
563 al., 2015). This later hypothesis is in accordance with studies showing an impact of  
564 dimerization on  $\beta$ -arrestins recruitment (Fillion et al., 2019). Differential effects of gp120  
565 on immobilization of CCR5 WT and L196K (**Figure 6**), compared to chemokines (**Figure**  
566 **5**), could also be explained by differences in recruitment of  $\beta$ -arrestins, linked to  
567 differences in the stabilized conformations of receptors.

568 Finally, our study suggested that CCR5 can be activated whether monomeric or dimeric.  
569 We showed that eGFP-CCR5-L196K, while mostly monomeric in its basal state (**Figure**  
570 **5B**), is still internalized (**Figure 5G**), suggesting that monomers can be activated, which  
571 is consistent with studies reporting that GPCR monomers can be active enough on their  
572 own to be functional (Whorton et al., 2007).

573 In summary, our single-particle tracking analysis established that a diversity of CCR5  
574 forms exists at the surface of living cells and that distinct ligands stabilize different  
575 receptors. This approach also revealed that receptor dimerization is involved in Gi  
576 protein-coupling in the basal state, and in the immobilization of receptors after activation,  
577 pointing out that receptor conformation regulates GPCRs signaling and fate after  
578 activation. In addition, our work suggested that the different receptor conformations likely  
579 engaged different ways of regulation, expanding GPCRs functions.

580

581 **Materials and Methods**

582

583 **Cell culture and reagents**

584 The HEK 293 cells stably expressing SNAP-FLAG-CCR5-WT and SNAP-FLAG-L196K  
585 and the A3.01 human T cell line stably expressing CCR5 (A3.01-R5) were previously  
586 described (Colin et al., 2013; Jin et al., 2018). These cell lines were maintained in  
587 Dubelcco's modified Eagle medium (DMEM) (Thermo Fisher Scientific) or RPMI 1640  
588 medium supplemented with 10 % Fetal Bovine Serum (FBS, GE Healthcare) and 100  
589 µg/ml penicillin/streptomycin (Life technologies).

590 The CCR5 inverse agonist maraviroc (MVC) was obtained from the National Institutes of  
591 Health. The native chemokine CCL4 was chemically synthesized by F. Baleux (Institut  
592 Pasteur, Paris, France). The chemokine analog PSC-RANTES (N- $\alpha$ -(n-nonanoyl)-des-  
593 Ser(1)-[L-thiopropyl(2), L cyclohexylglycyl(3)] RANTES(4-68)) was obtained through the  
594 Center for Aids reagents, National Institute for Biological Standards and Control (NIBSC,  
595 UK). The primary antibodies used are the anti-GFP (Roche), the anti-CCR5 2D7 mAb  
596 (BD-Biosciences); the anti-FLAG monoclonal antibodies M1 or M2 (Sigma-Aldrich).  
597 Secondary antibodies used were a phycoerythrin (PE)-conjugated anti-mouse antibody  
598 (BD Biosciences). The toxin from Bordetella pertussis (PTX) used at a 100 ng/ml  
599 concentration were from Sigma. The  $\beta$ arr1/2 siRNA (5'-ACCUGCGCCUCCGCUAUG-  
600 3') and a scrambled siRNA (control, 5'-UGGUUUACAUGUCGACUAA-3') (Dharmacon)  
601 were transfected by RNAimax (Invitrogen) according to the instructions of the  
602 manufacturer, as described (Jin et al., 2014). To select siRNA positive cells, cells were  
603 co-transfected with a plasmid coding the fluorescent protein mcherry (gift of F. Perez,  
604 Institut Curie). Soluble, monomeric HIV-1 glycoprotein gp120 was produced using a  
605 semliki forest virus (SFV) system as described (Benureau et al., 2016; Colin et al.,  
606 2018). The sequence coding for gp120 #25 and gp120 #34 were from PBMCs of

607 patients collected early after seroconversion or in the AIDS stage of infection,  
608 respectively (Colin et al., 2018). Recombinant soluble CD4 (sCD4), produced in S2 cell  
609 lines, was purified on a strep-Tactin column using the One-STrEP-tag fused to the CD4  
610 C-tail as a bait (production and purification of recombinant proteins technological  
611 platform, C2RT, Institut Pasteur).

#### 612 [Generation of cell lines](#)

613 The eGFP-CCR5 plasmid was a gift of F. Perez (Institut Curie, Paris, France)  
614 (Boncompain et al., 2019). The mutant eGFP-CCR5-L196K (substitution of L196 with a  
615 lysine) was generated by site-directed mutagenesis using the QuickChange II  
616 Mutagenesis kit (Agilent Technologies) according to the manufacturer's instruction. This  
617 mutant was verified by sequencing (Eurofins). HEK 293 cells stably expressing eGFP-  
618 CCR5-WT and HEK 293 cells stably expressing eGFP-CCR5-L196K were generated by  
619 calcium phosphate transfection and cultured for several weeks in 1 mg/ml G418  
620 (Geneticin, Invitrogen). Cell Clones were screened and sorted by flow cytometry (Attune  
621 NxT flow cytometer, Thermo Fisher) using an anti-GFP monoclonal antibody.

#### 622 [Receptor cell surface expression levels and internalization measured by flow cytometry](#)

623 Flow cytometry was used to quantitate the internalization of FLAG-SNAP-CCR5-WT  
624 compared to FLAG-SNAP-CCR5-L196K stably expressed in HEK 293 cells (Delhaye et  
625 al., 2007; Jin et al., 2018). We measured the levels of cell surface CCR5 stained with the  
626 anti-FLAG M2 antibody and with an anti-mouse coupled to phycoerythrin (PE) after  
627 chemokine treatment or not. Cells were incubated with a saturable amount of M2 for 45  
628 min to label receptors present at the plasma membrane, then incubated in the presence  
629 (or not) of 20 nM PSC-RANTES for the indicated time at 37°C. Cells were chilled to 4°C  
630 and stained with a PE conjugated anti-mouse IgG. Mean values were used to compute  
631 the proportion of internalized receptors as indicated by a decrease of immune-reactive

632 surface with PSC-RANTES compared with untreated cells. Cells were analyzed with  
633 Attune NxT flow cytometer (Thermo Fisher). At least 5,000 cells were analyzed per  
634 experiment using Kaluza software. Background was subtracted using the fluorescence  
635 intensity obtained on the parental HEK 293 cells.

#### 636 Chemotaxis

637 CCR5 expressing A3.01 cells (A3.01-R5,  $1.5 \times 10^5$ ), pre-treated or not with PTX (100  
638 ng/ml) during 3 h, in prewarmed RPMI-1640 supplemented with 20 mM HEPES and 1%  
639 serum, were added to the upper chambers of HTS-Transwell-96 Well Permeable  
640 Supports with polycarbonate membrane of 5  $\mu$ m pore size (Corning). PSC-RANTES  
641 (33.7 nM) or SDF-1 (control, 10 nM) was added to the lower chambers. Chemotaxis  
642 proceeded for 4 h at 37 °C in humidified air with 5% CO<sub>2</sub>. The number of cells migrating  
643 across the polycarbonate membrane was assessed by flow cytometry with Attune NxT  
644 flow cytometer (Thermo Fisher). Specific migration was calculated by subtracting  
645 spontaneous migration from the number of cells that migrated toward the chemokine.

#### 646 Live cell TIRF imaging

647 Round 25 mm No. 01 glass coverslips (Fisher Scientific) were pre-cleaned with 70%  
648 ethanol followed by acetone, with three consecutive washes in ddH<sub>2</sub>O.  $1.15 \times 10^5$  cells  
649 were plated onto pre-cleaned coverslips 72 h before imaging. Cells were imaged in TIRF  
650 medium (25 mM HEPES, 135 mM NaCl, 5 mM KCl, 1.8 mM CaCl<sub>2</sub>, 0.4 mM MgCl<sub>2</sub>,  
651 4.5 g/l glucose and 0.5% BSA, pH 7.4). Movies were acquired with an LSM 780 Elyra  
652 PS.1 TIRF microscope (Zeiss) equipped with an EMCCD Andor Ixon 887 1K camera,  
653 and using an alpha Pin Apo 100x/1.46 oil objective, a 488 nm (100 mW) HR solid laser  
654 line, and a BP 495-575 + LP 750 filter to detect eGFP-CCR5. Image acquisition was  
655 done at 1 frame / 33 msec (30 Hz) (100 to 200 frames), with 8 % (tracking) or 15 %  
656 (stoichiometrie) laser power at 37°C. Approximately 5-10 cells were acquired per

657 condition, per experiment. All live-imaging movies were analyzed using the open-source  
658 software Icy (Institut Pasteur).

#### 659 [Track analysis protocol](#)

##### 660 *Tracking receptors in TIRF imaging with Icy software*

661 To automatically detect eGFP-CCR5 tracks at the plasma membrane upon time, we  
662 used the software Icy (<http://icy.bioimageanalysis.org>) and the plugin *Spot tracking*,  
663 which reports their *xy* displacement and intensities, as previously described in Bertot *et al.*  
664 *(Bertot et al., 2018)*. *Spot tracking* was set to detect spots with approximately 3 pixels,  
665 and a threshold of 135. All other parameters were as default. Tracks were analyzed with  
666 the *Track manager* plugin. All data was exported to *Excel* for further analysis.

667 Tracks containing more than 10 % of virtual detections and more than three successive  
668 virtual detections were excluded from the track classification.

##### 669 *Splitting tracks into tracklets*

670 We deal with trajectories that have very different lengths and we want to estimate motion  
671 variations along the trajectory. Thus, we split all long tracks into several tracklets in order  
672 to better classify local motions. According to Section 1, this is done by setting  $N = 5$  and  
673 considering only the tracks with length larger than 6. Then, the different successive  
674 tracklets are defined by using the position between the  $(5k)^{\text{th}}$  and  $(5(k + 1))^{\text{th}}$  frame  
675 with  $k \geq 0$ .

##### 676 *Detecting immobile receptors*

677 To classify tracklets and identify distinct receptor dynamics, we first identified immobile  
678 receptors. In time lapse imaging, a tracklet  $X$  is defined by the vector of its successive  
679 positions at the different time frames  $X = (X_0, \dots, X_{N-1})$ , with  $N$  the length of the tracklet.

680 We considered that a receptor was immobile if

681

$$\max_{i \neq j=0, \dots, N-1} \|X_i - X_j\| < \sqrt{2} l$$

682 where  $l$  is the size of the object ( $l=2$  pixels typically). In other words, the previous  
683 criterion states that a tracklet is immobile if the maximal distance between two different  
684 positions is at most equal to the length of the diagonal of the square of edge  $l$ .

685 *The 3 types of motion of mobile receptors*

686 To classify the other tracklets corresponding to mobile receptors, we used the statistical  
687 method introduced in (Briane et al., 2018), which allows to distinguish three main types  
688 of motions:

689 (i) **Brownian motion**: the object (receptor) evolves freely and its trajectory is denoted by  
690  $\sigma B_t$  where  $\sigma$  is called the *diffusion coefficient*. The position of the object  $X_t$  at time  $t$  is  
691 given by  $X_t = X_0 + \sigma B_t$ . Brownian increments  $\sigma dB_t$  at each time are independent and  
692 normally distributed.

693 (ii) **Directed motion**: the object is actively transported by a deterministic force, and its  
694 motion can be modelled by the following stochastic differential equation:

$$dX_t = \mu dt + \sigma dB_t,$$

695 where  $\mu$  is a 2D-vector called *drift* and represents the deterministic force, and  $\sigma$  is the  
696 *diffusion coefficient* modelling the random Brownian motion.

697 (iii) **Confined motion**: the object is confined in a domain or evolves in an open but  
698 crowded area. This kind of motion can be modeled by an Ornstein-Uhlenbeck process:

$$dX_t = -\lambda(X_t - \mu)dt + \sigma dB_t.$$

700

701 We refer to (Durrett, 2018) for more properties about Brownian motion and stochastic  
702 calculus.

703 *Statistical classification of mobile tracklets*

704 The motion classification criterion defined in (Briane et al., 2018) essentially considers  
705 the ratio between the maximal distance from the initial point and the length of the  
706 tracklets. This can be evaluated by defining the following statistics

707

$$S(X, N) = \frac{\max_{i=0, \dots, N} |X_{t_i} - X_{t_0}|}{\left[ \frac{1}{2} \sum_{i=1}^N |X_{t_i} - X_{t_{i-1}}|^2 \right]^{\frac{1}{2}}}$$

708

709 where  $|\cdot|$  denotes the 2D-Euclidean norm. The classification is made by using the  
710 quantiles of order  $\alpha$  and  $1-\alpha$  ( $\alpha = 0.05$ ) of such a statistic for Brownian tracklets.

711 These quantiles, denoted by  $q(\alpha)$  and  $q(1-\alpha)$  respectively, depend on  $\alpha$  and  $N$ , and can  
712 be computed by Monte Carlo simulations (see (Briane et al., 2018)). This essentially  
713 consists in simulating a high number of Brownian tracklets, computing their statistics  
714 values and then evaluating the quantiles.

715 Then the tracklet motion is said to be confined if  $S(X, N) < q(\alpha)$ , directed if  $S(X, N) > q(1-\alpha)$ ,  
716 and Brownian otherwise. For  $N=5$  and  $\alpha = 0.05$ , we obtained  $q(\alpha) = 0.724$  and  $q(1-$   
717  $\alpha) = 2.464$ .

718 *From local classification of tracklet motion to global analysis of receptors' tracks*

719 The above statistical classifier allows estimating the local motion of each receptor. In a  
720 second time, we analyzed the difference of tracklet motions along the same longer  
721 receptor track. In particular, we evaluated if a receptor changed its type of motion along  
722 its trajectory.

723 Finally, our statistical framework for classifying tracklets motion provided a two-scales  
724 picture of the receptors' dynamic behavior: the classification of tracklets provided a



725 global estimation of receptors' motion, while the identified changes of receptors' motion  
726 along their full trajectories indicated the stability of each receptor's motion.

### 727 [Stoichiometry analysis](#)

728 Icy software was used to determine the intensity distribution of eGFP-spots. Spots were  
729 detected using the Spot detector wavelet-based algorithm (Olivo-Marin, 2002), and then  
730 converted to ROIs with 2 pixels radius. Data was exported to Excel. We observed a  
731 multimodal distribution of eGFP spots' intensities, and we decided to use the AIC  
732 criterion (Akaike information criterion) (Akaike, 1974) to uncover the number of modes in  
733 intensity distribution. Each mode putatively corresponds to a number of molecules.  
734 Therefore, statistical characterization of the multimodal distribution of eGFP spots'  
735 intensity will help to classify each spot with respect to its mode and, therefore, to its  
736 estimated number of molecules.

737 AIC analysis starts with the modeling of the empirical distribution  $e(x)$  of eGFP  
738 spots' intensities with a weighted sum of Gaussian laws,

$$e(x) = \sum_{i=1}^p \alpha_i N(\mu_i, \sigma_i)$$

739 where  $p$  is the number of Gaussian laws in the mixture,  $\alpha_i$  the weight of each law and  
740  $(\mu_i, \sigma_i)$  the corresponding mean and variance. For a fixed  $p$ , we first searched for the  
741 optimal parameters  $(\alpha_i^*, \mu_i^*, \sigma_i^*)$ , for  $i = 1..p$  that maximize the likelihood  $L$  of the model to  
742 the data:

743

$$L_p(\alpha_1, \mu_1, \sigma_1, \dots, \alpha_p, \mu_p, \sigma_p) = \prod_{j=1}^n \left[ \sum_{i=1}^p \frac{\alpha_i}{\sqrt{2\pi\sigma_i}} \exp\left(-\frac{(x_j - \mu_i)^2}{2\sigma_i}\right) \right]$$

744 where  $(x_1, x_2, \dots, x_n)$  are the observed eGFP intensities in the considered frame of the  
745 time-lapse sequence.

746 This first step of the AIC analysis provides the calibrated parameters  
747  $(\alpha_i^*, \mu_i^*, \sigma_i^*)_{i=1..p}$  when fitting a  $p$ -mixture model to data. Then, we computed the optimal  
748 number of modes  $p^*$  that would describe the different populations of eGFP spots with  
749 respect to their estimated number of molecules by minimizing the AIC:

$$AIC(p) = 2k_p - 2 \log(L_p^*)$$

750 where  $L_p^*$  is the maximized likelihood the  $p$ -mixture model, and  $k_p = 3p - 1$  is the  
751 number of free parameters of the  $p$ -mixture model.

## 752 **Acknowledgments**

753 We are grateful to Françoise Baleux (Institut Pasteur) and Franck Perez (Institut Curie)  
754 for the gifts of chemokines and plasmids. We acknowledge Oliver Hartley (University of  
755 Genova) and the Programme EVA Centre for AIDS Reagents for the chemokine  
756 derivative PSC-RANTES. We acknowledge Stéphane Petres from the Production and  
757 Purification of Recombinant Proteins (PPRP) platform (C2RT, Institut Pasteur) for sCD4  
758 production. We thank Audrey Salles from the Photonic BioImaging (PBI) platform  
759 (Imagopole) of Institut Pasteur for microscope maintenance and technical help. We  
760 thank Vannary Meas-Yedid Hardy (Institut Pasteur), Stéphane Dallongeville (BioImage  
761 Analysis Unit, Institut Pasteur), the Image Analysis Hub (C2RT, Institut Pasteur), and  
762 VizionR (Paris) for help with the image and data analysis.

763 This work was supported by grants from Agence National de Recherche sur le SIDA et  
764 les hépatites virales (ANRS), the French Government's Investissement d'Avenir program,  
765 Laboratoire d'excellence "Integrative Biology of Emerging Infectious Diseases" (grant  
766 ANR-10-LABX-62-IBEID), INCEPTION (ANR-16-CONV-0005) and France-BioImaging  
767 Infrastructure (ANR-10-INBS-04).

768 FM was the recipient of ANR-10-LABX-62-IBEID fellowship, G.N. of INCEPTION (ANR-  
769 16-CONV-0005) fellowship and P.C. of an ANRS fellowship.

770

771 **Competing Interests:** The authors declare that no competing interests exist.

772

773 **Author Contributions**

774 Fanny Momboisse, Conceptualization, Methodology, Validation, Formal analysis,  
775 Investigation, Writing - original draft preparation;

776 Giacomo Nardi, Conceptualization, Methodology, Software, Validation, Formal analysis,  
777 Writing - original draft preparation;

778 Philippe Colin, Validation, Formal analysis, Investigation;

779 Melany Hery, Validation;

780 Nelia Cordeiro, Validation;

781 Olivier Schwartz, Resources, Supervision, Funding acquisition;

782 Nathalie Sauvonnnet, Conceptualization, Formal analysis, Resources, Writing - original  
783 draft preparation, Funding acquisition;

784 Fernando Arenzana-Seisdedos, Resources, Supervision, Funding acquisition;

785 Thibault Lagache, Conceptualization, Methodology, Software, Formal analysis, Data  
786 curation, Writing - original draft preparation;

787 Bernard Lagane, Conceptualization, Formal analysis, Resources, Writing - original draft  
788 preparation, Supervision, Funding acquisition;

789 Jean-Christophe Olivo-Marin, Resources, Supervision, Funding acquisition;

790 Anne BreLOT: Conceptualization, Methodology, Validation, Formal analysis, Investigation,  
791 Resources, Data curation, Writing - original draft preparation, Visualization, Supervision,  
792 Project administration, Funding acquisition.

793

794 **List of Figure Supplement**

795 Figure1-figure supplement 1

796 Figure3-figure supplement 1

797 Figure4-figure supplement 1

798

799 **Videos Title**

800 **Video 1.** TIRF movie of a cell stably expressing eGFP-CCR5-WT acquired at 30 Hz. The  
801 region of interest was defined by the green line.

802 **Video 2.** TIRF movie of the same cell as in video 1 analyzed using the Icy software. Red  
803 circles correspond to the detection of bright spots using the *Spot detection* plugin.

804 **Video 3.** TIRF movie of the same cell as in video 1 and 2 analyzed using the Icy  
805 software and the *Spot tracking* plugin. Colored lines correspond to the tracked spots.

806 **Video 4.** TIRF movie acquired at 30 Hz of a cell stably expressing eGFP-CCR5-WT and  
807 treated by CCL4 (100 nM) for 14 min.

808 **Video 5.** TIRF movie acquired at 30 Hz of cells stably expressing eGFP-CCR5-WT and  
809 treated by PSC-RANTES (20 nM) for 3 min.

810 **Video 6.** TIRF movie acquired at 30 Hz of a cell stably expressing eGFP-CCR5-L196K  
811 and treated by PSC-RANTES (20 nM) for 2 min.

812

## 813 References

814

- 815 Abrol, R., Trzaskowski, B., Goddard, W. A., 3rd, Nesterov, A., Olave, I., & Irons, C. (2014).  
816 Ligand- and mutation-induced conformational selection in the CCR5 chemokine G  
817 protein-coupled receptor. *Proc Natl Acad Sci U S A*, 111(36), 13040-13045.  
818 <https://doi.org/10.1073/pnas.1413216111>
- 819 Ahn, D., Ham, D., & Chung, K. Y. (2021). The conformational transition during G protein-coupled  
820 receptor (GPCR) and G protein interaction. *Curr Opin Struct Biol*, 69, 117-123.  
821 <https://doi.org/10.1016/j.sbi.2021.03.013>
- 822 Akaike, H. (1974). A new look at the statistical model identification. *IEEE transactions on*  
823 *automatic control*, 19(6), 716-723.
- 824 Aldinucci, D., Borghese, C., & Casagrande, N. (2020). The CCL5/CCR5 Axis in Cancer  
825 Progression. *Cancers (Basel)*, 12(7). <https://doi.org/10.3390/cancers12071765>
- 826 Alkhatib, G., Combadiere, C., Broder, C. C., Feng, Y., Kennedy, P. E., Murphy, P. M., & Berger,  
827 E. A. (1996). CC CKR5: a RANTES, MIP-1 $\alpha$ , MIP-1 $\beta$  receptor as a fusion cofactor for  
828 macrophage-tropic HIV-1. *Science*, 272, 1955-1958.
- 829 Benureau, Y., Colin, P., Staropoli, I., Gonzalez, N., Garcia-Perez, J., Alcami, J., . . . Lagane, B.  
830 (2016). Guidelines for cloning, expression, purification and functional characterization of  
831 primary HIV-1 envelope glycoproteins. *J Virol Methods*, 236, 184-195.  
832 <https://doi.org/10.1016/j.jviromet.2016.07.019>
- 833 Berro, R., Klasse, P. J., Lascano, D., Flegler, A., Nagashima, K. A., Sanders, R. W., . . . Moore, J.  
834 P. (2011). Multiple CCR5 conformations on the cell surface are used differentially by  
835 human immunodeficiency viruses resistant or sensitive to CCR5 inhibitors. *J Virol*,  
836 85(16), 8227-8240. <https://doi.org/JVI.00767-11> [pii]10.1128/JVI.00767-11
- 837 Bertot, L., Grassart, A., Lagache, T., Nardi, G., Basquin, C., Olivo-Marin, J. C., & Sauvonnnet, N.  
838 (2018). Quantitative and Statistical Study of the Dynamics of Clathrin-Dependent and -  
839 Independent Endocytosis Reveal a Differential Role of EndophilinA2. *Cell Rep*, 22(6),  
840 1574-1588. <https://doi.org/10.1016/j.celrep.2018.01.039>
- 841 Boncompain, G., Herit, F., Tessier, S., Lescure, A., Del Nery, E., Gestraud, P., . . . Perez, F.  
842 (2019). Targeting CCR5 trafficking to inhibit HIV-1 infection. *Sci Adv*, 5(10), eaax0821.  
843 <https://doi.org/10.1126/sciadv.aax0821>
- 844 Bonsch, C., Munteanu, M., Rossitto-Borlat, I., Furstenberg, A., & Hartley, O. (2015). Potent Anti-  
845 HIV Chemokine Analogs Direct Post-Endocytic Sorting of CCR5. *PLoS One*, 10(4),  
846 e0125396. <https://doi.org/10.1371/journal.pone.0125396>
- 847 BreLOT, A., & Chakrabarti, L. A. (2018). CCR5 Revisited: How Mechanisms of HIV Entry Govern  
848 AIDS Pathogenesis. *J Mol Biol*, 430(17), 2557-2589.  
849 <https://doi.org/10.1016/j.jmb.2018.06.027>
- 850 Briane, V., Kervrann, C., & Vimond, M. (2018). Statistical analysis of particle trajectories in living  
851 cells. *Phys Rev E*, 97(6-1), 062121. <https://doi.org/10.1103/PhysRevE.97.062121>
- 852 Calebiro, D., Rieken, F., Wagner, J., Sungkaworn, T., Zabel, U., Borzi, A., . . . Lohse, M. J.  
853 (2013). Single-molecule analysis of fluorescently labeled G-protein-coupled receptors  
854 reveals complexes with distinct dynamics and organization. *Proc Natl Acad Sci U S A*,  
855 110(2), 743-748. <https://doi.org/1205798110> [pii]10.1073/pnas.1205798110
- 856 Chenouard, N., Bloch, I., & Olivo-Marin, J. C. (2013). Multiple hypothesis tracking for cluttered  
857 biological image sequences. *IEEE Trans Pattern Anal Mach Intell*, 35(11), 2736-3750.  
858 <https://doi.org/10.1109/TPAMI.2013.97>
- 859 Colin, P., Benureau, Y., Staropoli, I., Wang, Y., Gonzalez, N., Alcami, J., . . . Lagane, B. (2013).  
860 HIV-1 exploits CCR5 conformational heterogeneity to escape inhibition by chemokines.  
861 *Proc Natl Acad Sci U S A*, 110(23), 9475-9480. <https://doi.org/1222205110>  
862 [pii]10.1073/pnas.1222205110

- 863 Colin, P., Zhou, Z., Staropoli, I., Garcia-Perez, J., Gasser, R., Armani-Tourret, M., . . . Lagane, B.  
864 (2018). CCR5 structural plasticity shapes HIV-1 phenotypic properties. *PLoS Pathog*,  
865 *14*(12), e1007432. <https://doi.org/10.1371/journal.ppat.1007432>
- 866 de Chaumont, F., Dallongeville, S., Chenouard, N., Herve, N., Pop, S., Provoost, T., . . . Olivo-  
867 Marin, J. C. (2012). Icy: an open bioimage informatics platform for extended reproducible  
868 research. *Nat Methods*, *9*(7), 690-696. <https://doi.org/10.1038/nmeth.2075>
- 869 Delhaye, M., Gravot, A., Ayinde, D., Niedergang, F., Alizon, M., & BreLOT, A. (2007). Identification  
870 of a postendocytic sorting sequence in CCR5. *Mol Pharmacol*, *72*(6), 1497-1507.  
871 [http://www.ncbi.nlm.nih.gov/entrez/query.fcgi?cmd=Retrieve&db=PubMed&dopt=Citation](http://www.ncbi.nlm.nih.gov/entrez/query.fcgi?cmd=Retrieve&db=PubMed&dopt=Citation&list_uids=17855654)  
872 [&list\\_uids=17855654](http://www.ncbi.nlm.nih.gov/entrez/query.fcgi?cmd=Retrieve&db=PubMed&dopt=Citation&list_uids=17855654)
- 873 Deupi, X., & Kobilka, B. K. (2010). Energy landscapes as a tool to integrate GPCR structure,  
874 dynamics, and function. *Physiology (Bethesda)*, *25*(5), 293-303. <https://doi.org/10.1152/physiol.00002.2010>  
875 [pii]10.1152/physiol.00002.2010
- 876 Dorr, P., Westby, M., Dobbs, S., Griffin, P., Irvine, B., Macartney, M., . . . Perros, M. (2005).  
877 Maraviroc (UK-427,857), a potent, orally bioavailable, and selective small-molecule  
878 inhibitor of chemokine receptor CCR5 with broad-spectrum anti-human immunodeficiency  
879 virus type 1 activity. *Antimicrob Agents Chemother*, *49*(11), 4721-4732.  
880 [http://www.ncbi.nlm.nih.gov/entrez/query.fcgi?cmd=Retrieve&db=PubMed&dopt=Citation](http://www.ncbi.nlm.nih.gov/entrez/query.fcgi?cmd=Retrieve&db=PubMed&dopt=Citation&list_uids=16251317)  
881 [&list\\_uids=16251317](http://www.ncbi.nlm.nih.gov/entrez/query.fcgi?cmd=Retrieve&db=PubMed&dopt=Citation&list_uids=16251317)
- 882 Durrett, R. (2018). *Stochastic calculus: a practical introduction*. CRC press.
- 883 Escola, J. M., Kuenzi, G., Gaertner, H., Foti, M., & Hartley, O. (2010). CC chemokine receptor 5  
884 (CCR5) desensitization: cycling receptors accumulate in the trans-Golgi network. *J Biol*  
885 *Chem*, *285*(53), 41772-41780. <https://doi.org/10.1074/jbc.M110.153460> [pii]10.1074/jbc.M110.153460
- 886 Fillion, D., Devost, D., Sleno, R., Inoue, A., & Hebert, T. E. (2019). Asymmetric Recruitment of  
887 beta-Arrestin1/2 by the Angiotensin II Type I and Prostaglandin F2alpha Receptor Dimer.  
888 *Front Endocrinol (Lausanne)*, *10*, 162. <https://doi.org/10.3389/fendo.2019.00162>
- 889 Flanagan, C. A. (2014). Receptor conformation and constitutive activity in CCR5 chemokine  
890 receptor function and HIV infection. *Adv Pharmacol*, *70*, 215-263.  
891 <https://doi.org/10.1016/B978-0-12-417197-8.00008-0>
- 892 Fox, J. M., Kasproicz, R., Hartley, O., & Signoret, N. (2015). CCR5 susceptibility to ligand-  
893 mediated down-modulation differs between human T lymphocytes and myeloid cells. *J*  
894 *Leukoc Biol*, *98*(1), 59-71. <https://doi.org/10.1189/jlb.2A0414-193RR>
- 895 Garcia-Perez, J., Rueda, P., Staropoli, I., Kellenberger, E., Alcami, J., Arenzana-Seisdedos, F., &  
896 Lagane, B. (2011). New Insights into the Mechanisms whereby Low Molecular Weight  
897 CCR5 Ligands Inhibit HIV-1 Infection. *J Biol Chem*, *286*(7), 4978-4990.  
898 [http://www.ncbi.nlm.nih.gov/entrez/query.fcgi?cmd=Retrieve&db=PubMed&dopt=Citation](http://www.ncbi.nlm.nih.gov/entrez/query.fcgi?cmd=Retrieve&db=PubMed&dopt=Citation&list_uids=21118814)  
899 [&list\\_uids=21118814](http://www.ncbi.nlm.nih.gov/entrez/query.fcgi?cmd=Retrieve&db=PubMed&dopt=Citation&list_uids=21118814)
- 900 Gormal, R. S., Padmanabhan, P., Kasula, R., Bademosi, A. T., Coakley, S., Giacomotto, J., . . .  
901 Meunier, F. A. (2020). Modular transient nanoclustering of activated beta2-adrenergic  
902 receptors revealed by single-molecule tracking of conformation-specific nanobodies. *Proc*  
903 *Natl Acad Sci U S A*, *117*(48), 30476-30487. <https://doi.org/10.1073/pnas.2007443117>
- 904 Grove, J., Metcalf, D. J., Knight, A. E., Wavre-Shapton, S. T., Sun, T., Protonotarios, E. D., . . .  
905 Marsh, M. (2014). Flat clathrin lattices: stable features of the plasma membrane. *Mol Biol*  
906 *Cell*, *25*(22), 3581-3594. <https://doi.org/10.1091/mbc.E14-06-1154>
- 907 Irannejad, R., Tomshine, J. C., Tomshine, J. R., Chevalier, M., Mahoney, J. P., Steyaert, J., . . .  
908 von Zastrow, M. (2013). Conformational biosensors reveal GPCR signalling from  
909 endosomes. *Nature*, *495*(7442), 534-538. <https://doi.org/10.1038/nature12000>
- 910 Isbilir, A., Moller, J., Arimont, M., Bobkov, V., Perpina-Viciano, C., Hoffmann, C., . . . Lohse, M. J.  
911 (2020). Advanced fluorescence microscopy reveals disruption of dynamic CXCR4  
912 dimerization by subpocket-specific inverse agonists. *Proc Natl Acad Sci U S A*, *117*(46),  
913 29144-29154. <https://doi.org/10.1073/pnas.2013319117>



- 914 Jacquemard, C., Koensgen, F., Colin, P., Lagane, B., & Kellenberger, E. (2021). Modeling of  
915 CCR5 Recognition by HIV-1 gp120: How the Viral Protein Exploits the Conformational  
916 Plasticity of the Coreceptor. *Viruses*, 13(7). <https://doi.org/10.3390/v13071395>
- 917 Jin, J., Colin, P., Staropoli, I., Lima-Fernandes, E., Ferret, C., Demir, A., . . . Brelot, A. (2014).  
918 Targeting Spare CC Chemokine Receptor 5 (CCR5) as a Principle to Inhibit HIV-1 Entry.  
919 *J Biol Chem*, 289(27), 19042-19052. <https://doi.org/M114.559831>  
920 [pii]10.1074/jbc.M114.559831
- 921 Jin, J., Momboisse, F., Boncompain, G., Koensgen, F., Zhou, Z., Cordeiro, N., . . . Brelot, A.  
922 (2018). CCR5 adopts three homodimeric conformations that control cell surface delivery.  
923 *Sci Signal*, 11(529). <https://doi.org/10.1126/scisignal.aal2869>
- 924 Kasai, R. S., Ito, S. V., Awane, R. M., Fujiwara, T. K., & Kusumi, A. (2018). The Class-A GPCR  
925 Dopamine D2 Receptor Forms Transient Dimers Stabilized by Agonists: Detection by  
926 Single-Molecule Tracking. *Cell Biochem Biophys*, 76(1-2), 29-37.  
927 <https://doi.org/10.1007/s12013-017-0829-y>
- 928 Lagane, B., Ballet, S., Planchenault, T., Balabanian, K., Le Poul, E., Blanpain, C., . . . Bachelierie,  
929 F. (2005). Mutation of the DRY motif reveals different structural requirements for the CC  
930 chemokine receptor 5-mediated signaling and receptor endocytosis. *Mol Pharmacol*,  
931 67(6), 1966-1976. <https://doi.org/mol.104.009779> [pii]10.1124/mol.104.009779
- 932 Martinez-Munoz, L., Rodriguez-Frade, J. M., Barroso, R., Sorzano, C. O. S., Torreno-Pina, J. A.,  
933 Santiago, C. A., . . . Mellado, M. (2018). Separating Actin-Dependent Chemokine  
934 Receptor Nanoclustering from Dimerization Indicates a Role for Clustering in CXCR4  
935 Signaling and Function. *Mol Cell*, 71(5), 873. <https://doi.org/10.1016/j.molcel.2018.08.012>
- 936 Maurice, P., Daulat, A. M., Turecek, R., Ivankova-Susankova, K., Zamponi, F., Kamal, M., . . .  
937 Jockers, R. (2010). Molecular organization and dynamics of the melatonin MT(1)  
938 receptor/RGS20/G(i) protein complex reveal asymmetry of receptor dimers for RGS and  
939 G(i) coupling. *EMBO J*, 29(21), 3646-3659. <https://doi.org/10.1038/emboj.2010.236>
- 940 Moller, J., Isbilir, A., Sungkaworn, T., Osberg, B., Karathanasis, C., Sunkara, V., . . . Lohse, M. J.  
941 (2020). Single-molecule analysis reveals agonist-specific dimer formation of micro-opioid  
942 receptors. *Nat Chem Biol*, 16(9), 946-954. <https://doi.org/10.1038/s41589-020-0566-1>
- 943 Olivo-Marin, J.-C. (2002). Extraction of spots in biological images using multiscale products.  
944 *Pattern recognition*, 35(9), 1989-1996.
- 945 Patwardhan, A., Cheng, N., & Trejo, J. (2021). Post-Translational Modifications of G Protein-  
946 Coupled Receptors Control Cellular Signaling Dynamics in Space and Time. *Pharmacol*  
947 *Rev*, 73(1), 120-151. <https://doi.org/10.1124/pharmrev.120.000082>
- 948 Pierce, K. L., Premont, R. T., & Lefkowitz, R. J. (2002). Seven-transmembrane receptors. *Nat*  
949 *Rev Mol Cell Biol*, 3(9), 639-650. <https://doi.org/10.1038/nrm908>
- 950 Qian, H., Sheetz, M. P., & Elson, E. L. (1991). Single particle tracking. Analysis of diffusion and  
951 flow in two-dimensional systems. *Biophys J*, 60(4), 910-921.  
952 [https://doi.org/10.1016/S0006-3495\(91\)82125-7](https://doi.org/10.1016/S0006-3495(91)82125-7)
- 953 Salavessa, L., Lagache, T., Malarde, V., Grassart, A., Olivo-Marin, J. C., Canette, A., . . .  
954 Sauvonnnet, N. (2021). Cytokine receptor cluster size impacts its endocytosis and  
955 signaling. *Proc Natl Acad Sci U S A*, 118(37). <https://doi.org/10.1073/pnas.2024893118>
- 956 Scurci, I., Akondi, K. B., Pinheiro, I., Paolini-Bertrand, M., Borgeat, A., Cerini, F., & Hartley, O.  
957 (2021). CCR5 tyrosine sulfation heterogeneity generates cell surface receptor  
958 subpopulations with different ligand binding properties. *Biochim Biophys Acta Gen Subj*,  
959 1865(1), 129753. <https://doi.org/10.1016/j.bbagen.2020.129753>
- 960 Seyedabadi, M., Ghahremani, M. H., & Albert, P. R. (2019). Biased signaling of G protein coupled  
961 receptors (GPCRs): Molecular determinants of GPCR/transducer selectivity and  
962 therapeutic potential. *Pharmacol Ther*, 200, 148-178.  
963 <https://doi.org/10.1016/j.pharmthera.2019.05.006>
- 964 Shaik, M. M., Peng, H., Lu, J., Rits-Volloch, S., Xu, C., Liao, M., & Chen, B. (2019). Structural  
965 basis of coreceptor recognition by HIV-1 envelope spike. *Nature*, 565(7739), 318-323.  
966 <https://doi.org/10.1038/s41586-018-0804-9>

- 967 Sleno, R., & Hebert, T. E. (2018). The Dynamics of GPCR Oligomerization and Their Functional  
968 Consequences. *Int Rev Cell Mol Biol*, 338, 141-171.  
969 <https://doi.org/10.1016/bs.ircmb.2018.02.005>
- 970 Sohy, D., Yano, H., de Nadai, P., Urizar, E., Guillabert, A., Javitch, J. A., . . . Springael, J. Y.  
971 (2009). Hetero-oligomerization of CCR2, CCR5, and CXCR4 and the protean effects of  
972 "selective" antagonists. *J Biol Chem*, 284(45), 31270-31279.  
973 [http://www.ncbi.nlm.nih.gov/entrez/query.fcgi?cmd=Retrieve&db=PubMed&dopt=Citation](http://www.ncbi.nlm.nih.gov/entrez/query.fcgi?cmd=Retrieve&db=PubMed&dopt=Citation&list_uids=19758998)  
974 [&list\\_uids=19758998](http://www.ncbi.nlm.nih.gov/entrez/query.fcgi?cmd=Retrieve&db=PubMed&dopt=Citation&list_uids=19758998)
- 975 Sungkaworn, T., Jobin, M. L., Burnecki, K., Weron, A., Lohse, M. J., & Calebiro, D. (2017).  
976 Single-molecule imaging reveals receptor-G protein interactions at cell surface hot spots.  
977 *Nature*, 550(7677), 543-547. <https://doi.org/10.1038/nature24264>
- 978 Tabor, A., Weisenburger, S., Banerjee, A., Purkayastha, N., Kaindl, J. M., Hubner, H., . . .  
979 Gmeiner, P. (2016). Visualization and ligand-induced modulation of dopamine receptor  
980 dimerization at the single molecule level. *Sci Rep*, 6, 33233.  
981 <https://doi.org/10.1038/srep33233>
- 982 Tilton, J. C., Wilen, C. B., Didigu, C. A., Sinha, R., Harrison, J. E., Agrawal-Gamse, C., . . . Doms,  
983 R. W. (2010). A maraviroc-resistant HIV-1 with narrow cross-resistance to other CCR5  
984 antagonists depends on both N-terminal and extracellular loop domains of drug-bound  
985 CCR5. *J Virol*, 84(20), 10863-10876. <https://doi.org/10.1128/JVI.01109-10>
- 986 Vangelista, L., & Vento, S. (2017). The Expanding Therapeutic Perspective of CCR5 Blockade.  
987 *Front Immunol*, 8, 1981. <https://doi.org/10.3389/fimmu.2017.01981>
- 988 Veya, L., Piguat, J., & Vogel, H. (2015). Single Molecule Imaging Deciphers the Relation between  
989 Mobility and Signaling of a Prototypical G Protein-coupled Receptor in Living Cells. *J Biol*  
990 *Chem*, 290(46), 27723-27735. <https://doi.org/10.1074/jbc.M115.666677>
- 991 Whorton, M. R., Bokoch, M. P., Rasmussen, S. G., Huang, B., Zare, R. N., Kobilka, B., &  
992 Sunahara, R. K. (2007). A monomeric G protein-coupled receptor isolated in a high-  
993 density lipoprotein particle efficiently activates its G protein [Research Support, N.I.H.,  
994 Extramural Research Support, Non-U.S. Gov't Research Support, U.S. Gov't, Non-  
995 P.H.S.]. *Proc Natl Acad Sci U S A*, 104(18), 7682-7687.  
996 <https://doi.org/10.1073/pnas.0611448104>
- 997 Yanagawa, M., Hiroshima, M., Togashi, Y., Abe, M., Yamashita, T., Shichida, Y., . . . Sako, Y.  
998 (2018). Single-molecule diffusion-based estimation of ligand effects on G protein-coupled  
999 receptors. *Sci Signal*, 11(548). <https://doi.org/10.1126/scisignal.aao1917>

1000



## Figure supplement

### Single-molecule imaging reveals distinct effects of ligands on CCR5 dynamics depending on its dimerization status.

Fanny Momboisse<sup>1</sup>, Giacomo Nardi<sup>2</sup>, Philippe Colin<sup>3</sup>, Melany Hery<sup>1</sup>, Nelia Cordeiro<sup>1</sup>, Olivier Schwartz<sup>1</sup>, Nathalie Sauvonnnet<sup>5</sup>, Fernando Arenzana-Seisdedos<sup>4</sup>, Thibault Lagache<sup>2\*</sup>, Bernard Lagane<sup>3</sup>, Jean-Christophe Olivo-Marin<sup>2</sup>, Anne BreLOT<sup>1\*</sup>

Corresponding author: Anne BreLOT and Thibault Lagache

Anne BreLOT: [anne.brelot@pasteur.fr](mailto:anne.brelot@pasteur.fr)

Thibault Lagache: [thibault.lagache@pasteur.fr](mailto:thibault.lagache@pasteur.fr)

#### This PDF file includes:

Figure1-figure supplement 1  
Figure3-figure supplement 1  
Figure4-figure supplement 1  
Legends for Videos 1 to 6

#### Other materials for this manuscript include the following:

Video 1  
Video 2  
Video 3  
Video 4  
Video 5  
Video 6

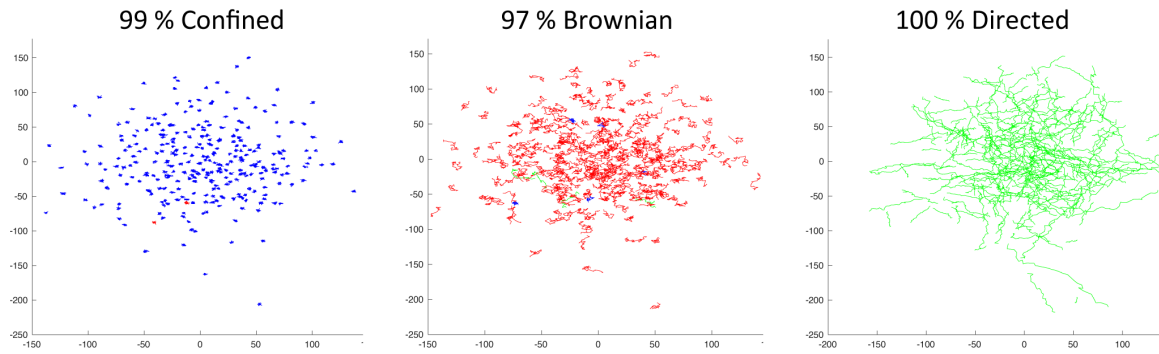


**Figure 1-figure supplement 1.** Validation of the statistical method using simulated trajectories. The three motions, confined, Brownian, and directed, were simulated by Monte Carlo experiments. For each type of motion, we simulated 300 tracks with length 11, with a Matlab program by using equations given in Materials and Methods. Trajectories were classified with the statistical method. The parameters used for the statistical classification were the following:  $N=10$ ,  $\alpha=0.05$ ,  $q(\alpha)=0.725$ , and  $q(1-\alpha) = 2.626$ . The percentage of detection of the different trajectories were indicated.

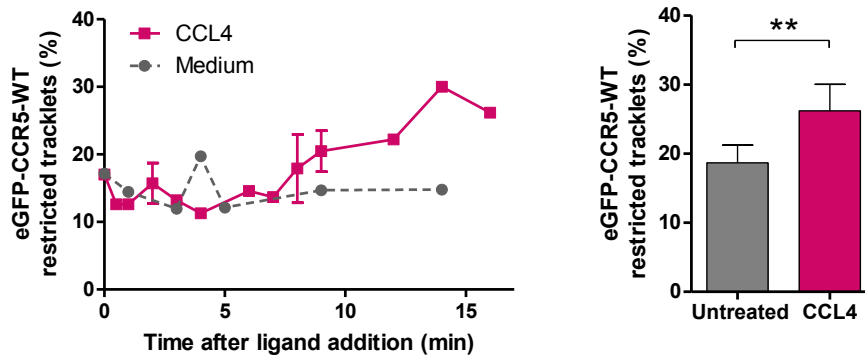


**Figure 3-figure supplement 1:** Effect of CCL4 on CCR5 mobility. eGFP-CCR5-WT expressing cells were treated or not with a saturating concentration of CCL4 (200 nM) and single particle tracking analysis was performed. Percentage of restricted tracklets after treatment over time (left) and after 12 to 16 min of treatment (right) (mean  $\pm$  SD,  $n = 9\,951$  and  $4\,320$  tracks for untreated and CCL4 conditions, from 6 and 3 cells respectively). Unpaired t test:  $p$  value  $0.0088^{**}$ .

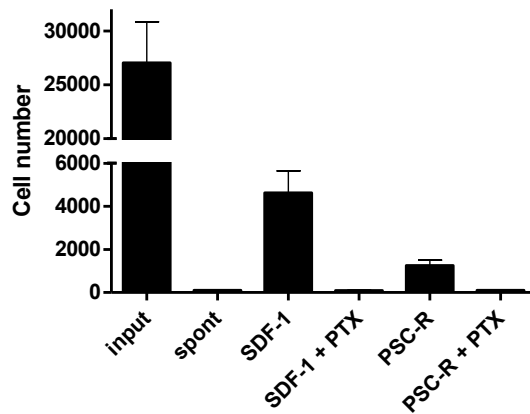


**Figure 4-figure supplement 1.** Effect of PTX treatment on chemokine-mediated chemotaxis. A3.01-R5 cells treated with 100 ng/ml PTX for 3 h were added to the upper chambers of HTS-transwell. Chemokines were to the lower chambers and chemotaxis were proceeded for 4 h. The number of cells migrating across the membrane was assessed by flow cytometry. PTX-treatment impaired SDF-1 (10 nM) and PSC-RANTES (33.7 nM)-mediated chemotaxis of A3.01-R5 cells. One representative experiment of 2 independent experiments (mean  $\pm$  SD of triplicates). *Spont*: Spontaneous migration (without chemokines in the lower chamber).

## Videos legends

**Video 1.** TIRF movie of a cell stably expressing eGFP-CCR5-WT acquired at 30 Hz. The region of interest was defined by the green line.

**Video 2.** TIRF movie of the same cell as in video 1 analyzed using the Icy software. Red circles correspond to the detection of bright spots using the *Spot detection* pluggin.

**Video 3.** TIRF movie of the same cell as in video 1 and 2 analyzed using the Icy software and the *Spot tracking* pluggin. Colored lines correspond to the tracked spots.

**Video 4.** TIRF movie acquired at 30 Hz of a cell stably expressing eGFP-CCR5-WT and treated by CCL4 (100 nM) for 14 min.

**Video 5.** TIRF movie acquired at 30 Hz of cells stably expressing eGFP-CCR5-WT and treated by PSC-RANTES (20 nM) for 3 min.

**Video 6.** TIRF movie acquired at 30 Hz of a cell stably expressing eGFP-CCR5-L196K and treated by PSC-RANTES (20 nM) for 2 min.